INTERNATIONAL ATOMIC ENERGY AGENCY
UNITED NATIONS EDUCATIONAL, SCIENTIFIC AND CULTURAL ORGANIZATION
INTERNATIONAL CENTRE FOR THEORETICAL PHYSICS
I.C.T.P., P.O. BOX 586, 34100 TRIESTE, ITALY, CABLE CENTRATOM TRIESTE

H4.SMR/449-38

WINTER COLLEGE ON
HIGH RESOLUTION SPECTROSCOPY

(8 January - 2 February 1990)

INSTABILITIES AND CHAOS IN SINGLE-MODE HOMOGENEOUS LINE LASERS

T. Arecchi & R.G. Harrison

(lecture given by R. Meucci)

Istituto Nazionale di Ottica
Firenze 50125 Arcetri
Italy

2. Instabilities and Chaos in Single-Mode Homogeneous Line Lasers

F.T. Arecchi

With 26 Figures

This chapter presents a review of the experimental investigation done in Florence on dynamical instabilities and deterministic chaos in Quantum Optics. In a dissipative system such as a laser we distinguish between a transient regime, strongly dependent on the initial conditions, and an asymptotic one, where the motion is confined on an attractor independent of the initial conditions. First, laser transients carry relevant information on the birth or death of a coherent state. Thus, a set of experiments is reported on the characterization of nonlinear transients and of their statistical features. Second, the onset of deterministic chaos is studied by referring to the invariant properties of low-dimensional attractors, in order to isolate the characteristics of chaos from the random fluctuations due to the coupling with a thermal reservoir. For this purpose, attention is focused on single-mode homogeneous-line lasers, whose dynamics is ruled by a low number of coupled variables. In the examined cases, experiments and theoretical model are in close agreement. In particular, when many attractors co-exist for the same parameter values (generalized multistability) the presence of random noise induces long lived transients with $1/f$ like low frequency spectra.

2.1 Background

Quantum optics from its beginning in 1960 with the first laser was considered as the physics of coherent and intrinsically stable radiation sources. Lamb's semiclassical theory [2.1] showed the role of the EM field in the cavity in ordering the phases of the induced atomic dipoles, thus giving rise to a macroscopic polarization and making possible a description in terms of very few collective variables. In the case of a single-mode laser and a homogeneous-gain line this meant just five coupled degrees of freedom, namely, a complex field amplitude E, a complex polarization P, and a population inversion ΔN. A corresponding quantum theory, even for the simplest model laser (the so called Dicke model, that is, a discrete collection of modes interacting with a finite number of two-level atoms) does not lead to a closed set of equations. However the interaction with other degrees of freedom acting as a thermal bath (atomic collisions, thermal radiation) provides truncation of high-order terms in the atom-field interation [2.2–4]. The problem may be reduced to five coupled

equations (the so-called Maxwell-Bloch equations) but now they are affected by noise sources to account for the coupling with the thermal bath [2.5]. Being stochastic, or Langevin equations, the corresponding solution in closed form refers to a suitable weight function or phase-space density. Anyway the average motion matches the semiclassical one, and fluctuations play a negligible role if one excludes the bifurcation points where there are changes of stability in the stationary branches. Leaving out the peculiar statistical phenomena which characterize the threshold points and which suggest a formal analogy with thermodynamic phase transitions [2.6] the main point of interest is that a single-mode laser provides a highly stable or coherent radiation field.

From the point of view of the associated information, the standard interferometric or spectroscopic measurements of classical optics, relying on average field values or on their first-order correlation functions, are insufficient. In order to characterize the statistical features of Quantum Optics it was necessary to make extensive use of photon statistics [2.7,8].

As discussed in detail in Sect. 2.3, coherence is equivalent to having a stable fixed point attractor and this does not depend on details of the nonlinear coupling, but on the number of relevant degrees of freedom. Since such a number depends on the time scales on which the output field is observed, coherence becomes a question of time scales. This is the reason why for some lasers coherence is a robust quality, persistent even in the presence of strong perturbations, whereas in other cases coherence is easily destroyed by the manipulations common in the laboratory use of lasers, such as modulation, feedback or injection from another laser.

This chapter is a review of the simplest variety of instabilities and chaos on active Quantum Optics. Precisely, Sect. 2.2 explores transient instabilities, related to the decay of an initial unstable state, Sect. 2.3 is a general presentation of low-dimensional chaos in lasers, including the description of the relevant measurements upon which any assessment on chaos has to rely. Sections 2.4–7 describe the investigations developed at Istituto Nazionale di Ottica, Firenze, and are respectively devoted to lasers with modulated losses, lasers with injected signals, lasers with feedback and bidirectional ring lasers. For convenience, mathematical derivations are collected in an appendix.

2.2 Transient Decay Toward a Stable State

As will be discussed in the next section, the notion of chaotic dynamics is based on the geometric properties of the attractor. This is defined heuristically as the locus of the phase space of a dissipative system where any initial condition asymptotically merges. For a more formal definition, see [2.9]. The simplest dynamical systems are the stable ones, where the attractor is just one point (as in a coherent laser) or two points (as in a bistable device) or a finite number of points (as in a multistable system). In such a case it is interesting to study the transient instability as the system precipitates from a generic initial condition toward the attracting fixed point.

A nonequilibrium system, under the action of external parameters, may undergo a transition in the sense that one (or a set) of its macroscopic observables have a sizeable change. Usually these changes are studied by a slow variation of the external parameter, in order to measure the stationary fluctuations and their associated spectra around each equilibrium point.

More dramatic evidence on the decay of an unstable state can be obtained by applying sudden jumps to the driving parameter and observing the statistical transients. The decay is initiated by microscopic fluctuations. In the first linear part of the decay process the fluctuations are amplified, hence during the transient, and until nonlinear saturation near the new stable point reduces them, fluctuations do not scale with the reciprocal of the systems size, as it is at equilibrium.

An experiment on the photon statistics of the laser field during its switch initiated this investigation [2.10]. Figures 2.1–3 give the transient photon statistics during a laser build-up and the associated average photon number and variance.

Similar experiments were afterward done on gas-liquid or magnetic transitions, and received the name of spinodal decomposition [2.11].

Limiting to the case of one stochastic amplitude x, the most natural approach was to measure the probability density $P(x,t)$ at a given time t after the sudden jump of the driving parameter. A time-dependent solution in terms of an eigenfunction expansion is unsuitable for the large number of terms involved, with the exception of small jumps near threshold [2.12] or the asymptotic behavior for long times.

Solving for the moments $\langle x^k(t)\rangle$ leads to an open hierarchy of coupled equations. A two-piece approximation [2.13] consists in first letting the system decay from the unstable point under the linearized part of the deterministic force, diffusing simultaneously because of the stochastic forces. This yields a

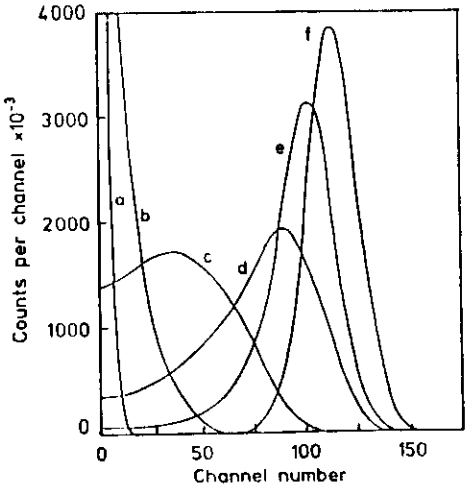

Fig. 2.1. Experimental statistical distributions with different time delays obtained on a laser transient. All distributions are normalized to the same area *(a)* 2.6 μs, *(b)* 3.7 μs, *(c)* 4.3 μs, *(d)* 5 μs, *(e)* 5.6 μs, *(f)* 8.8 μs

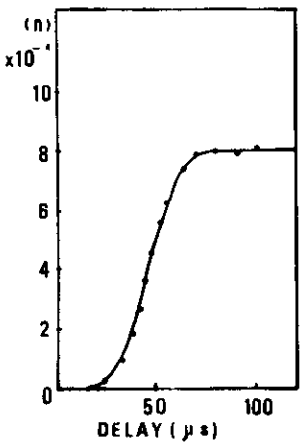

Fig. 2.2. Evolution of the average photon number $\langle n \rangle$ inside the cavity as a function of the time delay

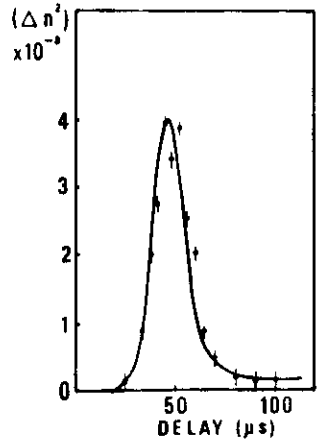

Fig. 2.3. Evolution of the variance $\langle \Delta n^2 \rangle$ of the statistical distribution of photons inside the cavity, as a function of the time delay

short-time probability distribution of easy evaluation. Then we solve for the nonlinear deterministic path and spread it over the ensemble of initial conditions previously evaluated in the linear regime.

A different approach leads instead to closed moment equations of easy solution [2.14,15]. We consider the time t, at which a given threshold z_F is crossed, as the stochastic parameter, whose distribution $Q(t, z, z_F)$ in terms of the interval between the initial position z and z_F must be assigned. Here the time is no longer an ordering parameter but an interval limited by a start-stop operation. Let the position z get unstable under a force $F(z)$ and a noise delta-correlated with a correlation $D(z)$. Then the evaluation of the moment $T_m \equiv \langle t^m \rangle$ is given by a simple recurrence formula as [2.14]

$$F(z)T'_m + D(z)T''_m = -mT_{m-1} \tag{2.1}$$

(the apex denoting differentiation with respect to z).

When we apply this formalism to the decay of unstable states, since D scales with the inverse system size, we can expand the results in D series and display the first relevant correction to the deterministic solution. We find for the mean time T_1

$$T_1(z) = \int_z^{z_F} \frac{dy}{F(y)} + \int_z^{z_F} dy \frac{dF}{dy} \frac{D}{F^3} \ , \tag{2.2}$$

where the first term on the right-hand side is the deterministic part. For a spread in the initial position z, $T_1(z)$ should still be averaged over the set of z.

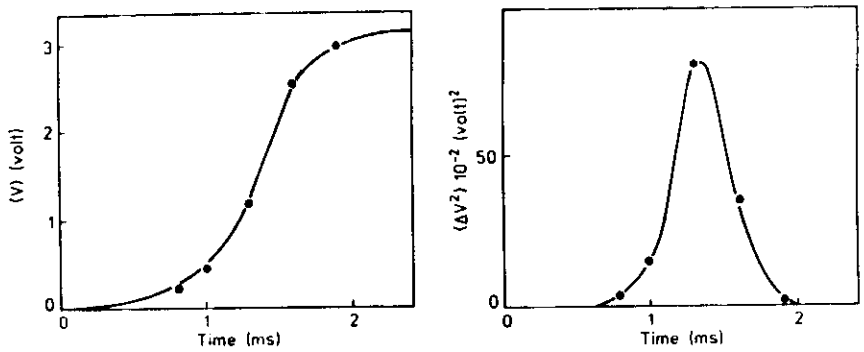

Fig. 2.4. Transient statistical evolution of an electron oscillator driven from below to above threshold by a sudden jump. No external noise added. Average amplitude V and variance. *Dots* denote experiment and *solid line* denotes theory

Similarly, performing the same approximation for T_2 we obtain for the variance $\Delta T \equiv T_2 - T_1^2$ the following relation

$$\Delta T = 2 \int_z^{z_F} dy \frac{D(y)}{F^3(y)} \ . \tag{2.3}$$

In order to show the power of this approach, we have measured the crossing time probability distributions for an electronic oscillator driven from below to above threshold [2.15].

Figure 2.4 gives the mean oscillator amplitude and its variance versus time as in the usual stochastic treatment of transients, Fig. 2.5 gives the variance of crossing times for increasing threshold as defined here.

The following comments convey some of the relevant physics: (i) the first term of (2.2) yields an average decay time which scales as $T_1 \approx \ln(N)$, that is, a logarithmic divergence with the system size N; (ii) a constant variance for increasing threshold means that the various trajectories are shifted versions of the same deterministic curve, and the noise scaling as $1/N$ plays a role only in spreading the initial condition; (iii) introduction of an external noise adds a fluctuation peculiar for each path, giving a ΔT dependent on z_F.

In conclusion, this new experimental characterization of a statistical transient shows a clear separation between the role of the initial spread and the noise along each path. In the case of superfluorescence, a delay time statistics in the pulse onset with respect to the preparation time has offered the most detailed tools for a comparison between measurements [2.16] and the corresponding theory [2.17].

Similar considerations apply also to bistable or multistable situations [2.15] and have been recently re-considered with specific reference to optical bistability [2.18].

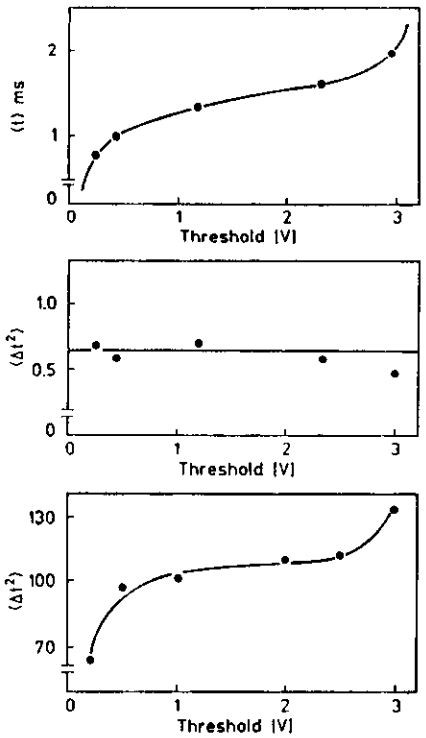

Fig. 2.5a–c. Transient oscillator as in Fig. 2.4. Statistical distribution of the time intervals between the initial condition and the crossing time (a), variance under the action of the internal noise (b), variance for an added external noise (c). In (b) and (c) the scale is in units of $10^{-9}\,s^2$. *Dots* denote experimental and *solid line* denotes theory

2.3 Deterministic Chaos

2.3.1 Historical Aspects

Until recently the current point of view as that of few-body dynamics was fully predictable, and that only addition of noise sources, due to coupling with a thermal reservoir, could provide statistical fluctuations. Lack of long-time predictability, or turbulence, was considered as resulting from the interaction of a large number of degrees of freedom, as in a fluid above the critical Reynolds number (Landau-Hopf model of turbulence).

On the contrary, it is now known that even in systems with few degrees of freedom nonlinearities may give rise to expanding directions in phase space and this, together with the lack of precision in assigning initial conditions, is sufficient to induce a loss of predictability over long times.

This level of dynamical description was born with the three-body problem in celestial mechanics (Poincare). Already a three-body dynamic system is very different from the two-body problem since, in general, there are asymptotic instabilities. This means a divergence, exponential in time, of two phase space trajectories stemming from nearby initial points. The uniqueness theorem for solutions of differential systems seems to offer an escape way: be more and more precise in localizing the coordinates of the initial point. However a fundamental difficulty arises. Only rational numbers can be assigned by a finite number of digits. A "precise" assignment of a real number requires an infinite acquisition time and an infinite memory capacity to store it, and neither of these two infinities is available to the physicist. Hence any initial condition implies a truncation. A whole range of initial conditions, even if small, is usually given and from within it trajectories may arise whose difference becomes sizeable after a given time, if there is an exponental divergence. This means that predictions are in general limited in time and that motions are complex, starting already from the three-body case. In fact, we know nowadays from very elementary topological considerations that a three-dimensional phase space corresponding to three coupled degrees of freedom is already sufficient to yield a positive Lyapunov exponent, and accordingly an expanding phase-space direction. This complexity is not due to coupling with a noise source as a thermal reservoir, but to sensitive dependence on initial conditions. It is called determinstic chaos.

The birth of this new dynamics was motivated by practical problems, such as fixing the orbit of a satellite or forecasting meteorology [2.19], and it was strongly helped by the introduction of powerful computers. The mathematics of multiple bifurcations leading from a simple behavior to a complex one is under current investigation. Some regularities, such as the "scenarios" [2.10] or routes to deterministic chaos, have already been explored. We are hopefully on the verge of a new formalism, which will describe in a unified way the passage from order to complicated behaviors such as developed turbulence in a fluid.

2.3.2 Dynamical Aspects

A dissipative system (i.e., with damping terms) does not conserve the phase-space volume. If we start with initial conditions confined in a hypersphere of radius ϵ, that is, with an initial phase volume

$$V_0 = \epsilon^N$$

as time goes on, the sphere transforms into an ellipsoid with each axis modified by a time dependent factor. Its volume is

$$V_t = \epsilon^N \exp\left(\Sigma_i \lambda_i t\right)$$

(λ_i: Lyapunov exponents). Since the volume has to contract, $V_t < V_0$, then

$$\Sigma_i \lambda_i < 0 \ . \tag{2.4}$$

We denote the sequence of λ exponents, starting from the smallest up to the highest as the Lyapunov spectrum. Let us consider for simplicity just the signs of nonzero λ_i, keeping the zero for $\lambda_i = 0$. We then describe a sequence of, negative, zero and positive λ_i as, e.g., $(--0+)$. For $N = 1$, we have $(-)$ and a

segment $V_0 = \epsilon^1$ of initial conditions shrinks to a single point for $T \to \infty$, that is, the attractor is a fixed point. For $N = 2$ the system goes either to a fixed point $(--)$, or to a limit cycle (-0). Chaotic motion $[(-+)$ with $\lambda_+ < |\lambda_-|]$ is forbidden in two dimensions by the Poincaré-Bendixon theorem. For $N = 3$, besides fixed point $(---)$, and limit cycle $(--0)$, we can have motion on a torus with two incommensurate frequencies (-00), but we can also have $(-0+)$, that is, a positive λ which gives an expanding direction along which we rapidly get uncertainty.

An example of chaotic motion is offered by the Lorenz model of hydrodynamic instabilities [2.19] which corresponds to the following equations where the parameter values have been chosen in order to yield one positive Lyapunov exponent:

$$\begin{aligned} \dot{x} &= -10x + 10y \ , \\ \dot{y} &= -y + 28x - xz \ , \\ \dot{z} &= -(8/3)z + xy \ . \end{aligned} \tag{2.5}$$

The above considerations suggest the system will exhibit low-dimensional chaos, with the simplest phase-space topology allowing for the appearence of a positive Lyapunov exponent.

Focusing on these situations in quantum optics permits close comparison between experiments and theory. By purpose, I do not tackle the vast class of inhomogeneously broadened lasers, where it is extremely difficult to drive close correspondences between experiments [2.21] and theory [2.22] because of the large number of coupled degrees of freedom (Sect. 2.2.2).

If we couple Maxwell equations with Schrödinger equations for N atoms confined in a cavity, and expand the field in cavity modes, keeping only the first mode E which goes unstable, this is coupled with the collective variables P and Δ describing the atomic polarization and population inversion as follows, see (2.A.5)

$$\begin{aligned} \dot{E} &= -kE + gP \ , \\ \dot{P} &= -\gamma_\perp P + gE\Delta \ , \\ \dot{\Delta} &= -\gamma_\parallel(\Delta - \Delta_0) - 4gPE \ . \end{aligned} \tag{2.6}$$

For simplicity, we consider the cavity frequency at resonance with the atomic resonance, so that we can take E and P as real variables and we have three coupled equations. Here, k, $\gamma_\perp$, $\gamma_\parallel$ are the loss rates for field, polarization and population, respectively, g is a coupling constant and Δ_0 is the population inversion which would be established by the pump mechanism in the atomic medium, in the absence of coupling. While the first equation comes from Maxwell equations, the two others imply the reduction of each atom to a two-level atom resonantly coupled with the field, that is, a description of each atom in a isospin space of spin 1/2. The last two equations are like Bloch equations which describe the spin precession in presence of a magnetic field. For such a reason (2.6) are called Maxwell-Bloch equations.

The presence of loss rates means that the three relevant degrees of freedom are in contact with a "sea" of other degrees of freedom. In principle, (2.6) could be deduced from microscopic equations by statistical reduction techniques [2.5]. A simple derivation is shown in the Appendix 2.A.

The similarity of Maxwell-Bloch equations (2.6) with Lorenz equations (2.5) would suggest the easy appearence of chaotic instabilities in single-mode, homogeneous-line lasers. However, time-scale considerations rule out the full dynamics of (2.6) for most of the available lasers. Equations (2.5) have damping rates which lie within one order of magnitude of each other. On the contrary, in most lasers the three damping rates are wildly different from one another.

The following classification has been introduced [2.23]

Class A (e.g., He-Ne, Ar, Kr, dye): $\gamma_\perp \simeq \gamma_\parallel \gg k$. The two last equations of (2.6) can be solved at equilibrium (adiabatic elimination procedure) and one single nonlinear field equation describes the laser. $N = 1$ means fixed point attractor, hence coherent emission.

Class B (e.g., ruby, Nd, CO): $\gamma_\perp \gg k \lesssim \gamma_\parallel$. Only polarization is adiabatically eliminated (middle equation of (2.6)) and the dynamics is ruled by two rate equations for field and population. $N = 2$ allows also for period oscillations.

Class C (e.g., FIR lasers) $\gamma_\parallel \approx \gamma_\perp \approx k$. The complete set of (2.6) has to be used, hence Lorenz like chaos is feasible (Chap. 5).

We have carried a series of experiments on the birth of deterministic chaos in CO_2 lasers (class B). In order to increase, by at least 1, the number of degrees of freedom, we have tested the following configurations:

i) Introduction of a time dependent parameter to make the system non autonomous [2.24]. Precisely, an electro-optical modulator modulates the cavity losses at a frequency near the proper oscillation frequency Ω provided by a linear stability analysis, which for a CO_2 laser happens to lie in the 50–100 KHz range, providing easy and accurate sets of measurements.

ii) Injection of a signal from an external laser detuned with respect to main one, choosing the frequency difference near the above mentioned Ω. With respect to the external reference the laser field has two quadrature components which represent two dynamical variables. Hence we reach $N = 3$ and observe chaos [2.23].

iii) Use a bidirectional ring, rather than a Fabry-Perot cavity [2.25]. In the latter case the boundary conditions constrain the forward and backward waves, by phase relations on the mirror, to act as a single standing wave. In the former case forward and backward waves have just to fill the total ring length with an integer number of wavelengths but there are no mutual phase constrains, hence they act as two separate variables. Furthermore, when the

field frequency is detuned with respect to the center of the gain line, a complex population grating arises from interference of the two counter-going waves, and as a result the dynamics becomes rather complex, requiring $N>3$ dimensions.

iv) Add an overall feedback, besides that provided by the cavity mirrors, by modulating the losses with a signal provided by the output intensity [2.26]. If the feedback has a time constant comparable with the population decay time, it provides a third equation sufficient to yield chaos.

Notice that while methods (i), (ii) and (iv) require an external device, (iii) provides intrinsic chaos. In any case, since feedback, injection or modulation are currently used in laser applications, the evidence of chaotic regions puts a caution on the optimistic trust in the laser coherence.

Of course, the requirement of three coupled nonlinear equations does not necessarily restrict attention to just the Lorenz equations. In fact, none of the explored case (i to iv) corresponds to Lorenz chaos.

2.3.3 Information Aspects

Here, we discuss what we measure to assess chaos. We plot two of the three (or more) variables on a plane phase-space projection. This way, we build projections of phase space trajectories on an $x-y$ oscilloscope. Simultaneously we can measure the power spectrum. In Sect. 2.4 a sequence of subharmonic bifurcations are shown, which eventually leads to an intricated trajectory (strange attractor) and to a continuous power spectrum. But how can we discriminate between deterministic chaos and noise? After all, noise also would give a continuous spectrum, and the phase space point would fill ergodically part of the plane, thus covering a two-dimensional set.

In order to discriminate deterministic chaos from order as well as from random noise, we introduce two invariants of the motion, one static the other dynamic.

We partition the phase space into small boxes of linear size ε and give ith box a probability $p_i = M_i/M$ equal to fractional number of times it has been visited by the trajectory. This way, we build a Shannon information $I(\varepsilon)$, and with it an "information dimension" $D_1(\varepsilon)$ [2.27] which is, in general, a fractional number, or a "fractal":

$$I(\varepsilon) = -\sum_i p_i \log p_i \ , \tag{2.7}$$

$$D_1(\varepsilon) = -\lim_{\varepsilon\to 0} \frac{I(\varepsilon)}{\log \varepsilon} \ . \tag{2.8}$$

To understand the meaning of a fractal, look up an operational definition of dimension [2.28]. Let us compare three sets: (i) a segment of unit length; (ii) the Cantor set, built by taking out the middle one-third of the unit segment and repeating the operation on each fragment; (iii) the Koch curve, built by replacing the middle third with the other two sides of an equilateral triangle and repeating the operation add infinitum. At each stage of the partition, we cover each set with beads of suitable size not to lose in resolution (e.g., diameter $1/3$ at the first partition) and count the number N for each set (at the first partition, we need 2 for the Cantor set, 3 for the segment, 4 for the Koch curve). We define the fractal dimension as the ratio

$$D_0(\varepsilon) = \frac{\log N(\varepsilon)}{\log 1/\varepsilon} \ . \tag{2.9}$$

This definition is independent of the partition. Indeed, for the Cantor set and the Koch curve we have $N=2$, $\varepsilon = 1/3$ and $N=4$, $\varepsilon = 1/3$, respectively, at the first partition, yielding

$$D_0(\text{Cantor}) = \frac{\log 2}{\log 3} \simeq 0.63\ldots \ , \quad \text{and}$$

$$D_0(\text{Koch}) = \frac{\log 4}{\log 3} \simeq 1.2618\ldots \ .$$

At the second partition the number of necessary beads goes as N^2 and the diameter of each as ε^2, hence D_0 remains invariant.

Going back to the information dimension $D_1(\varepsilon)$ we see that we have replaced $\log N$ with $I(\varepsilon)$ which is an *average* [for p_i all equal, we recover $I(\varepsilon) = \log N$]. Hence D_1 generalizes D_0 whenever the density of points is not uniform along the trajectory.

As D_0 was independent of the partition stage, similarly D_1 is an invariant, but static (time does not enter). It can be shown that $D_0 \geq D_1$, however for non pathological sets the difference is irrelevant. Let us refer for simplicity to an $N=3$-dimensional phase space. If $D=0$ (fixed point) or 1 (limit cycle) or 2 (torus) we have an ordered, or coherent, motion. In the other limit of random noise, fluctuations fill ergodically an N dimensional region of the space, hence $D=3$. Deterministic chaos has to be in between, that is

$$2<D<3 \ .$$

Hence, a fractal dimension is an indicator of chaos. As we show later, this indicator is expressed in term of correlation functions thus, it requires the same measuring techniques introduced in photon statistics.

These features related to the topology of the attractor have a temporal counterpart in another invariant, which measures how information is dissipated in a motion to maintain knowledge on the system. To build this dynamic invariant, we partition both space and time in boxes of sizes ε and τ that we name $i_1, i_2, \ldots i_d$ at each of the discrete times $\tau, 2\tau, \ldots d\tau$, and introduce the joint probability over the d time intervals,

$$p_{i_1 i_2 \ldots i_d} \equiv \{x(t=\tau) \subset i_1 ; \ldots ; x(t=d\tau) \subset i_d\} \ .$$

Correspondingly, we define a joint information

$$I_d(\varepsilon) = -\sum_{(i_1 \ldots i_d)} p_{i_1 \ldots i_d} \log p_{i_1 \ldots i_d} \ . \tag{2.10}$$

Then, by a limit operation, define the Kolmogorov entropy as the rate of information loss per unit time

$$K \equiv \lim_{\tau \to 0} \lim_{\varepsilon \to 0} \lim_{d \to \infty} \frac{1}{d\tau} \sum_{n=1}^{d} (I_{n+1} - I_n) = \lim \frac{1}{d\tau} I_d \ . \tag{2.11}$$

Now we have two indicators to gauge the difference among *order, random noise* (Brownian motion) and *deterministic chaos*. Referring to K, it is easily seen that

$K = 0$ for order (no information loss) ;

$K = \infty$ for random noise (total information loss) ;

$0 < K < \infty$ for deterministic chaos .

The box counting method desribed above is impractical. It may require 10^6 points for a convergent numerical result. On the contrary, the following method introduced by *Grassberger* and *Procaccia* [2.29] is applicable to only 10^3–10^4 independent data points. We generalize Shannon information defining the order-f information as

$$I_f(\varepsilon) = \frac{1}{1-f} \ln \sum_i p_i^f \ . \tag{2.12}$$

For $f \to 1$ we recover the usual definition. Associated with I_f, there is an order-f dimension of the attractor

$$D_f = \lim_{\varepsilon \to 0} \frac{I_f(\varepsilon)}{\ln 1/\varepsilon} \ . \tag{2.13}$$

For $f = 0$ and 1 we recover D_0 and D_1. Consider $f = 2$. The sum $\sum p_i^2$ is just the probability that a pair of random points on the attractor fall into the same box, that is, that two arbitrary points will have a distance less than ε. Calling this probability $C(\varepsilon)$, we expect thus

$$C(\varepsilon) = \lim_{N \to \infty} \frac{1}{N^2} \sum_{ij} \theta(\varepsilon - |\boldsymbol{x}_i - \boldsymbol{x}_j|) \simeq \varepsilon^{D_2} \tag{2.14}$$

where $C(\varepsilon)$ is measured as the number of pairs (i, j) with a distance $|\boldsymbol{x}_i - \boldsymbol{x}_j| < \varepsilon$. In (2.14), θ is the Heaviside step function.

Experimentally, we do not measure at each time the vector $\boldsymbol{x}(t)$ of phase space, but just one component $x_i(t)$ (for instance, just the light out of a laser).

However, in a nonlinear system, any component $x_k(t)$ will influence x_i at a later time (no normal mode transformation !). Hence, we can build an m-dimensional phase space $\xi(t)$ by just measuring one single component x_i at successive times and considering the m-fold as a single point in m space:

$$\xi(t) \equiv [x_i(t), x_i(t + \tau), \ldots x_i(t + (m-1)\tau)] \ . \tag{2.15}$$

As we evaluate the slope $\log C$ vs $\log \varepsilon$ from our data, we can stop from increasing m when the slope shows saturation. The saturated slope is D_2.

2.3.4 Role of Transients: The Hyperchaos

Nonlinear dissipative systems can have many simultaneously coexisting basins of attraction (generalized multistability – GM). This situation can be destabilized by changes of the control parameters, merging two independent attractors into a single one via an intermediate region which is only sporadically visited near the transition. The associated dynamics implies a low frequency tail (deterministic diffusion) [2.30]. Vice versa, when the above coexistence is stable, application of external noise may induce jumps between two otherwise disjoint regions of phase space.

The simultaneous presence of deterministic chaos and noise should not introduce new features within one attractor, since trajectories are already irregular. When however many attractors coexist for the same parameters, addition of noise makes it possible to leave a basin and go to another (which would be otherwise forbidden by the uniqueness theorem). This "hyperchaos" gives rise to low frequency spectra of $1/f$ type.

Clear evidence of generalized multistability was first shown in an electronic oscillator [2.31] and then in the modulated laser [2.24]. In both cases, besides the qualitative appearance of different attractors in phase space, there was a low-frequency spectral component due to noise-induced jumps among different attractors. Both measurements, however, might be considered as experimental artifacts. In fact, there is evidence of single attractors made of two sub-regions with infrequent passages from one to the other (see, e.g., the Lorenz attractor). In such a case, the low-frequency tail corresponds to the sporadic passages, and does not require added noise, (deterministic diffusion). As a matter of fact, power spectra do not permit discrimination between the two phenomena.

An analysis of the role of noise in GM was given for a cubic iteration map, allowing for two simultaneous attractors [2.32a], and in the numerical studies of a forced Duffing oscillator with a double potential well, in a parameter region allowing for the simultaneous existence of more than one attractor [2.32b].

A recent solution of the $1/f$ spectral problem [2.33] is based on the double randomness due to both the irregular deterministic motion with long lived transients, where the trajectory wanders near a fractal basin boundary, and the presence of stochastic noise. In this case, $1/f$ behavior can be accurately traced over more than three decades in frequency.

2.4 The Modulated Laser

For a single-mode (class B) laser tuned at the center line, the phase space becomes two-dimensional, see (2.A.17). However introduction of a time-dependent parameter makes the system non autonomous adding a third equation, see (2.A.16), thus making possible the appearence of a positive Lyapunov exponent. It is then a pratical matter to localize the values of the control parameters (pump, modulation frequency and amplitude) for which this will occur.

When we apply a time-dependent loss the evolution follows (2.A.16,17) given as

$$\begin{aligned} \dot{I} &= 2kI(z-1) \ , \\ \dot{z} &= \gamma_{\|}(z_0 - z - zI) \ , \\ \dot{k} &= mk_1\Omega \sin \Omega t \ . \end{aligned} \tag{2.16}$$

For $m \to 0$, we have small deviations from the equilibrium values

$$\begin{aligned} \bar{I} &= z_0 \quad 1 \ , \\ \bar{z} &= 1 \ . \end{aligned} \tag{2.17}$$

These deviations are linear in m and synchronous with the external frequency Ω. Destabilization of this limit cycle has to be dealt with by the Floquet theory [2.34]. It may be shown that even for $m \to 0$ a nonlinear resonance yields a positive Lyapunov exponent for Ω around the characteristic frequency given by the imaginary part of (2.A.21), that is

$$\Omega \simeq \sqrt{2k_1\gamma_{\|}(z_0 - 1)} \ . \tag{2.18}$$

For a CO_2 laboratory laser near threshold $k \sim 3 \times 10^7 s^{-1}$, $\gamma_{\|} \sim 10^4 s^{-1}$, and $z_0 - 1 \sim 0.1$ (10% above threshold), the corresponding frequency $f = \Omega/2\pi$ is in the 50 kHz range, easily accessible.

Thus we have made two series of experimental observations, the first [2.24] devoted to an experimental assessment of chaotic instabilities by phase-space portraits and power spectra, the second [2.35] to fractal dimensions and Kolmogorov entropy.

The driving frequency f was chosen to vary in the region from $\Omega/2\pi$ to its third harmonic, that is from 60 to 190 kHz. We have explored modulation values between 1% and 5%. A complete state diagram would yield the dynamical features for all possible values of the modulation parameters m and Ω. However, the strip $m = 1\%$–5% does not display m dependence; therefore we limit ourselves to giving experimental results at $m = 1\%$ for various Ω values.

The experimental setup consists of a CO_2 laser carefully stabilized against thermal and acoustic disturbances, with the discharge current stabilized to better than $1/10^4$. No long-term stabilization was necessary. The electro-optical modulator was a CdTe, antireflex-coated, 6-cm-long crystal, with an absorption less than 0.2%. The laser cavity includes also a $\lambda/4$ plate and a beam expander, both coated to limit the total losses per pass to 20%. The laser output is detected on a fast (2.5-ns rise time) pyroelectric detector whose current, proportional to the photon number $n(t)$, is sent together with its time derivative $\dot{n}(t)$ to an $x-y$ scope, in order to have the phase-space portrait $(n, \dot{n})$. The detector is also sent to a Rockland spectrum analyzer to measure the power spectra. The limited range (up to 100 kHz) of the spectrum analyzer limited the frequency range explored in this first run. We show later that interesting bifurcations are also expected in 180-kHz domain.

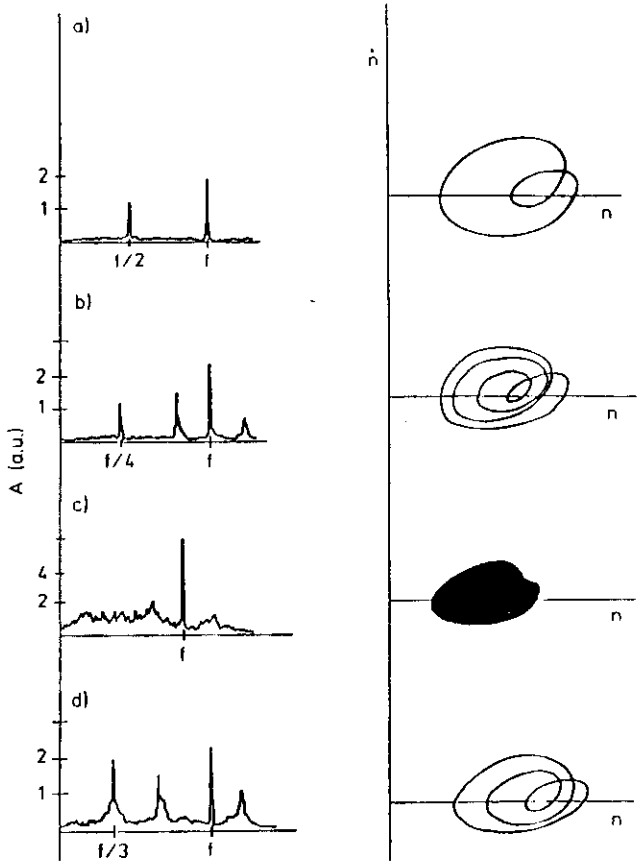

Fig. 2.6. Experimental phase-space portraits (n – n') *(right side)* and the corresponding frequency spectra *(left side)* for different modulation frequencies f. *(a)* $f = 62.75$ kHz. Period-two limit cycle and corresponding $f/2$ subharmonic. *(b)* F – 63.80 kHz. Period-four limit cycle and $f/4$ subharmonic. *(c)* $f = 64.00$ kHz. The phase-space portrait shows a strange attractor (the oscilloscope spot could not resolve single windings). The power spectrum is a quasicontinuous one with a small peak at the modulation frequency (see the scale change with respect to previous figures). *(d)* f – 64.13 kHz. Period-three limit cycla and $f/3$ subharmonic

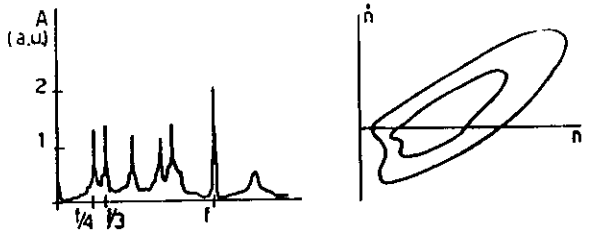

Fig. 2.7. $f = 63.85\,\text{kHz}$. Experimental evidence of generalized multistability (coexistence of two independent attractors). The power spectrum shows that those attractors correspond to $f/3$ and $f/4$ subharmonic bifurcations, respectively; in phase space, the multiple windings merged within the thickness of the phase portrait contour

In Fig. 2.6 we show experimental data in a narrow region between 62.7 and 64.25 kHz where various bifurcations occur. This region is limited above andbelow by wide intervals with stable single-period limit cycles. Figure 2.6a shows the $f/2$ bifurcation at $f = 62.7\,\text{kHz}$, Fig. 2.6b the $f/4$ case for $f = 63.8\,\text{kHz}$; Fig. 2.6c exhibits the strange attractor and a broad-band spectrum for $f = 64.0\,\text{kHz}$; and Fig. 2.6d displays the $f/3$ case for $f = 64.2\,\text{kHz}$. Furthermore, at $f = 63.85\,\text{kHz}$ a new feature appears, namely the coexistence of two independent stable attractors, one of period $4(f/4)$ and the other of period $3(f/3)$ (Fig. 2.7). This bistable situation has nothing to do with the common optical bistability where two dc output amplitude values appear for a single dc driving amplitude. We call this coexistence of two attractors "generalized bistability" (Sect. 2.3.4).

In Figs. 2.8 and 9 we report the theoretical equivalents of Figs. 2.6 and 7, respectively, obtained by computer solution of (2.16) with parameter values in the range of the experiment.

As stated in Sect. 2.3, $1/f$ type low-frequency divergences, with power spectra as $f^{-\alpha}$ ($\alpha = 0.6$–1.2), appear when the following conditions are fulfilled: (i) There are at least two basins of attraction; (ii) the attractors have become strange and any random noise (always present in a macroscopic system) acts as a bridge, triggering jumps between them. These jumps have the $f^{-\alpha}$ feature. In the region of bistability (Fig. 2.7) we have increased the modulator amplitude m up to the point where the two attractors have become strange. Figure 2.10 shows the sudden increase in the low-frequency spectrum. The divergent part has a power-law behavior $f^{-\alpha}$ with $\alpha \approx 0.6$.

The above described first run is still affected by the experimental uncertainties which characterize a phase space projection or a power spectrum. Does the first one show a self-similar structure beyond the chaotic threshold, as theoretically expected for a strange attractor, or does it just fill ergodically a two-dimensional region of $(n, \dot{n})$ plane, thus being trivial random noise? After all the latter test (continuous frequency spectrum) is also a common property of random noise and it is not a sufficient characterization of deterministic chaos.

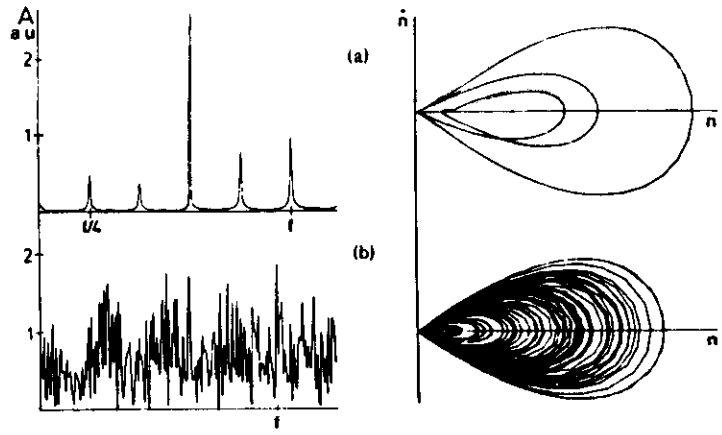

Fig. 2.8. Computer plots for the parameter values $\gamma_{\parallel} = 10^5\,\text{s}^{-1}$, $k = 7 \times 10^7\,\text{s}^{-1}$, $m = 2.0 \times 10^{-2}$, $\Delta_0 = 2.0 \times 10^{11}$. *(a)* $f = 64.33\,\text{kHz}$. Subharmonic bifurcation $f/4$, as in the experiment of Fig. 2.6b. *(b)* $f = 78.8\,\text{kHz}$, $m = 3 \times 10^{-2}$. Strange attractor and broad spectrum corresponding to a chaotic solution

In order to set a more reliable distinction between chaos and random noise, and also to specify the route to chaos (Fig. 2.6 is only a preliminary evidence of a Feigenbaum, n subharmonic, route), we have improved the stability of our system. This time, a stable $f/8$ subharmonic frequency and even an $f/10$ periodic window inside the chaotic region have been observed. To give an idea of the reliability of the apparatus we report here a series of behaviors observed at 2% modulation depth for slight changes of the modulation frequency, controlled via a programmable synthesizer driven by a microprocessor. In the following

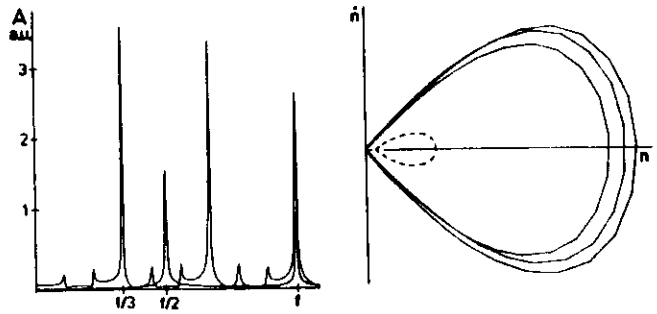

Fig. 2.9. Theoretical generalized bistability; $f = 119.0$ kHz, $m = 2.0 \times 10^{-2}$. The phase-space portrait shows the existence of two independent attractors, corresponding to the subharmonic frequencies $f/2$ (---) and $f/3$ (——); relative spectra are superimposed. It must be noted that one attractor remains inside the other as in the experiment of Fig. 2.7. If initial conditions are properly changed, a third attractor is found with a subharmonic frequency $f/10$ (not plotted for the sake of simplicity). Initial conditions: $n_0 = 4 \times 10^8$, $\dot{n}_0 = 0$ (---), $n_0 = 2 \times 10^5$, $\dot{n}_0 = -2 \times 10^6$ (——)

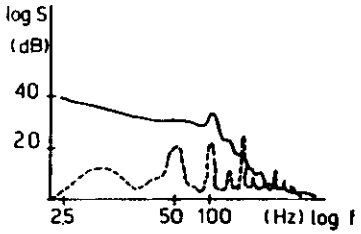

Fig. 2.10. Experimental power spectra in the case of two attractors, stable (---), and strange (—)

sequence the number is the set frequency (in kHz), and then the relevant subharmonics are indicated: 191 290, $f/5$ and $f/4$; 191 313, $f/3$ and $f/4$; 191 320, $f/2$ and f; 191 324, f; 191 327, $f/2$ and $f/3$; 191 331, $f/3$; 191 337, $f/4$. This is just a sample from a much larger data collection.

As we keep the modulation frequency constant at 191 000 kHz and increase the modulation depth from 1 % to 20 %, the system passes through a period-doubling cascade up to the accumulation point and enters a fully chaotic region. The chosen frequency is close to the third harmonic of the nonlinear laser resonance Ω. As we scanned the frequency we found a narrow tongue of maximum sensitivity around 3Ω, where the laser destabilizes with the least amount of modulation.

The signal was digitized by a LeCroy transient recorder with 32 000 samples in memory. Setting the internal clock at 320 ns, we obtained approximately 16 points for each period of the fundamental frequency with light-bit resolution. By synchronizing the sampling time to the external drive period we obtained a projection of the Poincaré section. The projection is onto a one-dimensional space (we measure only the intensity) independent of the other variables. In Fig. 2.11 we present the sections and the corresponding time series, respectively. The advantage of this signal processing is that we are able to analyze a high number of perods (32 000 maximum) with a single acquisition. Furthermore, it allows a much larger-bandwidth processing of narrow pulse sequences, which otherwise requires a high sampling rate with the related problems in data storing and processing. In Fig. 2.11, on the left-hand side, the band width is 300 kHz, and on the right it is 100 MHz; indeed we can notice already in the $f/8$ plot a loss of resolution in the smaller peaks on the left-hand side.

We analyze digitized time sequences of the laser output intensity and reconstruct the attractors with an embedding technique. For the determination of the fratal dimension we follow the method of Grassberger-Procaccia.

If we define $N_n(\varepsilon)$ as the number of vectors whose distance is smaller than ε, andif the embedding dimension n is large enough, then $N_n(\varepsilon) \sim \varepsilon^{\nu}$, where ν is the D_2 dimension of the attractor. In Figs. 2.12a to f we plot log $N_n(\varepsilon)$ as a function of log ε for a sequence of bifurcations $f/4$, $f/8$, and chaos. We limit our analysis to the regions where the slope remains constant over a wide region of log ε and where it is independent of n, as it must be from theoretical predictions.

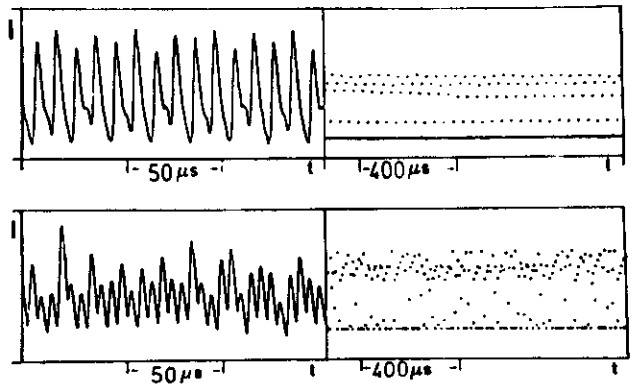

Fig. 2.11. *Top:* Laser intensity vs time for an $f/8$ subharmonic frequency, and corresponding stroboscopic intensity plot with the time interval between successive pints equal to the period of the modulation frequency (191 000 kHz). *Bottom:* Laser intensity vs time and stroboscopic plot for chaotic behavior. The period of the modulation is 5.2 μs. We note on the left-hand side the loss of resolution due to the limited acquisition bandwidth. This drawback is absent on the right-hand side because of the huge increase in band width

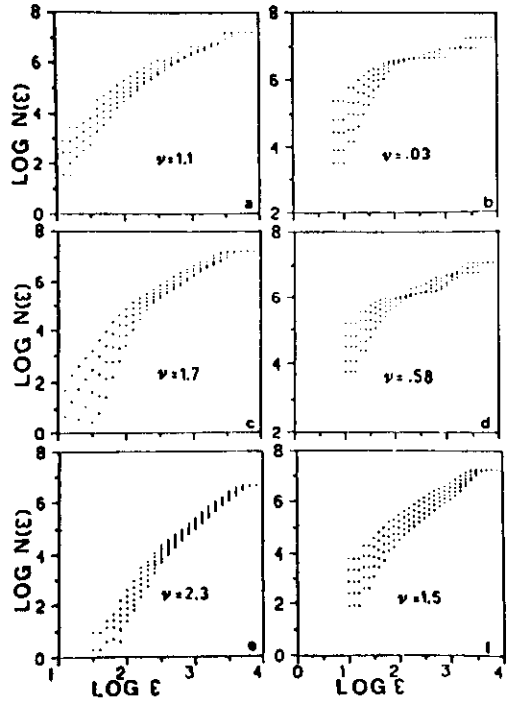

Fig. 2.12. Plots of log $N_n(\varepsilon)$ vs log ε for different values of n calculated from the time series (*left hand panels*) and from the stroboscopic sections (*right hand panels*) for different subharmonic frequencies *(a), (b)* $f/4$; *(c), (d)* $f/8$; and *(e), (f)* chaotic behavior. All best-fit values of the slope ν are assimed to have an overall estimated error of ±0.1. 6000 points were used. The embedding dimensions for all reported plots run from 5 to 9. Dimensions from 1 to 15 were tested

From inspection of Figs. 2.12a and b it is clear that the slope obtained for the $f/4$ subharmonic saturates at $\nu \sim 1$ in the time series and $\nu \sim 0$ in the Poincaré section. For the $f/8$ subharmonic ν is slightly above 1.5 (Figs. 2.12c and d). This result, even though not readily understandable because the time signal still appears periodic, nevertheless agrees with the theoretical prediction for the dimension at the accumulation point (infinite periodicity) of the logistic map ($1.5376 < \nu < 1.53385$). Indeed this dimension has been proven to be universial for those mappings for which the Feigenbaum scaling law holds [2.36]. We present here a heuristic interpretation based on our data. In our expermental system, the unavoidable noise yields a trajectory wandering over a nonzero range of parameter values, thus "testing" near by periodic attractors of the subharmonic sequence. For infinite resolution, we would see for the stroboscopic data a staircase of horizontal plateaus each with zero slope, as it appears at higher embedding dimensions in Figs. 2.12b and d. However, the finite resolution of the correlation measurements averages over adjacent steps, and thus provides the 0.58 slope, as it appears in Fig. 2.12d. This is the first time that the dimension at the accumulation point of a Feigenbaum cascade has been measured in an experimental system.

When the system enters the chaotic region, the fractal dimension suddenly jumps to a higher value ($\nu = 2.4$).

The time behavior of the intensity obtained by numerical integration of (2.16) was processed in the same manner as the experimental signal. Figure 2.13 shows the results obtained for an $f/8$ solution and a strange attractor. Again near the accumulation point $\omega \sim 1.5$. Direct comparison of Fig. 2.13 with Figs. 2.12c and d shows a good agreement between experiment and model.

It is important to stress that this agreement between theory and experiment is obtained with no floating parameters, but just by feeding (2.16) with the values, for our CO_2 laser and the frequency and amplitude of loss modulation as in the experiment, that is, the frequency set at 191 000 kHz and $m = 2.0\,\%$ and 2.85 %, respectively, for the left and right-hand sides of Fig. 2.13.

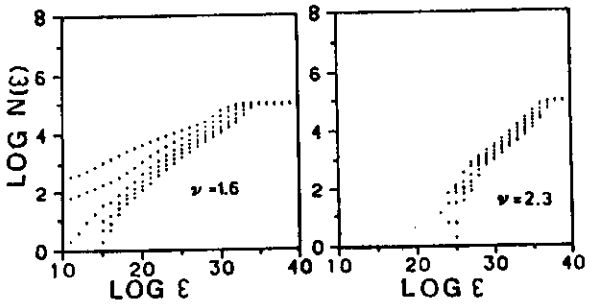

Fig. 2.13. Plots of log $N(\varepsilon)$ vs log ε for different dimensions n obtained from the numerical integration of themodel equations for two different cases, $f/8$ subharmonic (*left-hand side*) and chaos (*right-hand side*). 6000 points were used

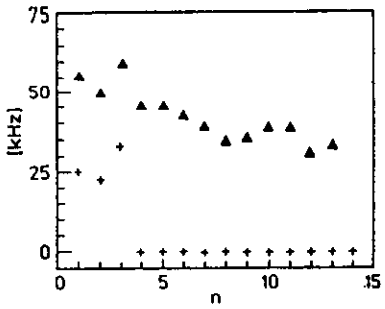

Fig. 2.14. Correlation entropy K_2 (in kHz) vs the embedding dimension for the $f/4$ (+ + +) and the chaotic ($\triangle\triangle\triangle$) attractor

The high regularity of the stroboscopic $N(\varepsilon)$ plots for increasing the embedding dimension suggests evaluation of an approximation to the Kolmogorov entropy. In Fig. 2.14 we report the correlation entropy K_2 versus the embedding dimension for the $f/4$ and for the chaotic attractor, versus the embedding dimension, from the data of Fig. 2.12. We see that while $K_2 = 0$ for $f/4$, $K_2 \simeq 35$ kHz for the chaotic attractor. As we have a single positive Lyapunov exponent and as the embedding time is 5.2 μs, we estimate that the half-loss of information corresponds to 3.8 periods of the modulation frequency.

2.5 The Laser with Injected Signal (LIS)

Injecting an external signal into a single-mode laser provides an extra degree of freedom. Indeed, in general, the field amplitude x has to be decomposed into two dynamical variables, that is, the two quadrature components $x_1 + ix_2 = x$ with respect to the external phase reference. In class C lasers this provides a fourth equation [2.37,38] which is more than the necessary requirement for deterministic chaos. A simpler situation is that of a class B LIS, which is ruled by (2.A.24) that we repeat here for convenience

$$\begin{aligned} \dot{I}/2k &= Iz(1+\delta^2)^{-1} - I + \sqrt{I}x_0 \cos\varphi \ , \\ \dot{\varphi}/k &= -\vartheta - \delta z(1+\delta^2)^{-1} - x_0 \sin\varphi/\sqrt{I} \ , \\ \dot{z}/\gamma_{\|} &= z_0 - z - zI(1+\delta^2)^{-1} \ . \end{aligned} \tag{2.19}$$

The frequency relations among gain line, cavity, external field and internal lasers are given in Fig. 2.15.

Equation (2.A.25) yields a steady state relation between output and input intensity that shows bistability (Fig. 2.16). For each $\bar{I}$ value in Fig. 2.16, the other two steady-state variables are given by

$$\bar{z} = z_0 \frac{1+\delta^2}{1+\delta^2+\bar{I}} \ , \tag{2.20}$$

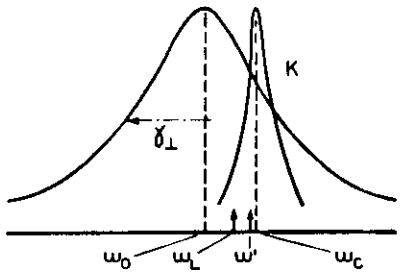

Fig. 2.15. Qualitative plot of the frequency relations among atomic resonance (homogeneous width $\gamma_\perp$) centered at ω_0, cavity resonance (width k) centered at ω_c, and injected field at ω_I

$$\bar{\varphi} = \arccos \frac{\sqrt{\bar{I}}}{x_0}\left(\frac{x_0}{1+\delta^2+\bar{I}} - 1\right) . \tag{2.21}$$

The hysteresis amount depends on both detunings (Fig. 2.16). The lower part of the bistable curve is always unstable. The upper part is wholly stable for zero detuning ($\theta - \delta = 0$). For nonzero detuning, it has a stable locked region and an unstable one where the laser oscillates either regularly or irregularly. We have observed two different ways to reach the locked regime, either by decreasing the oscillation frequency (tangent bifurcation), or by decreasing the amplitude of oscillation (Hopf bifurcation), and two different routes to chaos, either by intermittency or by period doubling.

An extensive linear stability analysis was reported in [2.39], together with numerical solutions of (2.19) for different values of the injected amplitude $A = x_0$ and mutual detuning $\theta - \delta$. Some results are summarized below.

In Fig. 2.17 we show regular oscillations in the output intensity; the higher frequency is that predicted by the linear stability analysis, while the lower one is related to a spiking – with amplitudes which can also be ten or more times higher than the steady state – due to field injection. As a matter of fact we have found that in this region, when the injecting amplitude is too low to lock the system steadily, the laser operates for most part of the time at ω_1 (external frequency) but it regularly unlocks going to ω_L (internal frequency). During

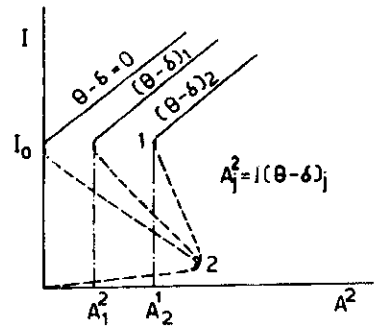

Fig. 2.16. Steady-state solution for LIS equations. Output intensity versus intensity of the injected field for constant value of the pump parameter (x_0) and different values of the detuning ($\omega_1 - \omega_L$). The *dashed line* shows the unstable region and the *solid line* shows the region where the steady-state solutions are stable. For each curve, the critical value of the intensity of the injected field is marked with A_j^2. For A^2 larger than A_j^2, there is no instability

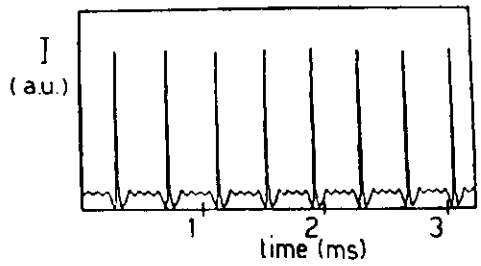

Fig. 2.17. LIS: Spiking and regular oscillations in the output intensity vs time

the oscillation at ω_L the energy of the injecting field enhances the population inversion so that it gives rise, with a delay related to the injecting intensity, to a giant pulse. Increasing the injecting amplitude, the frequency of these pulses goes to zero, because the system remains locked for longer times.

In Fig. 2.18 we show the temporal sequence which leads to chaos, on changing $x_0 = A$, by intermittency. Each dot representing the peak of an oscillation, we see, from bottom to top, how the laminar period becomes shorter and shorter and eventually dies in a wholly developed chaos.

The bifurcation sequence is shown in Fig. 2.19. The bifurcation occurs in the higher spikes while between two near-lying higher peaks we find oscillations at Ω.

Preliminary experimental data have been obtained by a three-laser set-up [2.40], the first laser being a ring laser where the dynamics develops, the second one the external injecting laser and the third one a master oscillator with

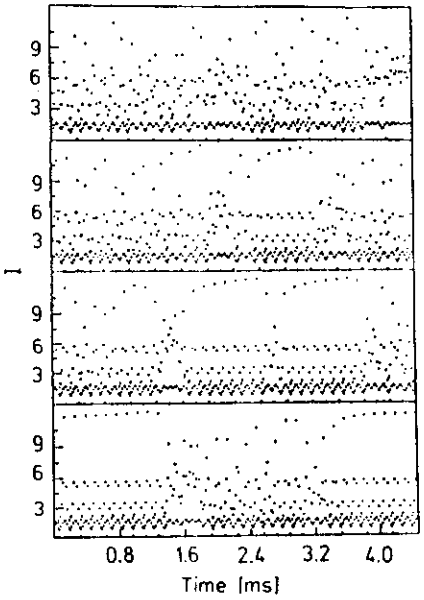

Fig. 2.18. LIS: Temporal sequence leading to chaos by intermittency increasing A (from *bottom* to *top*), each dot representing a maximum

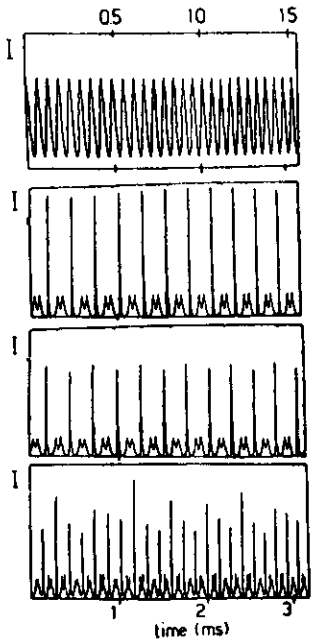

Fig. 2.19. LIS: Output intensity vs time. A is increased from top to bottom and chaos is reached by frequency doubling in the higher peaks

reference to which first and second laser are stabilized. The parameter region explored in this experiment was sufficient to yield oscillatory instabilities but not enough to reach chaos.

2.6 Instabilities in a Laser with Feedback

In laser applications where high stability is required, an overall negative feedback is currently used, besides that already provided by the electromagnetic cavity, for instance by controlling the pump strength with a signal provided by the detected output intensity [2.41]. Such a feedback is not just an added artifact, but it affects, in a fundamental way, the dynamics of photon generation; indeed, it has been proposed [2.42a] as a mean to provide squeezed states of the electromagnetic field, and preliminary evidence of such an effect has been given [2.42b]. However, a fundamental objection to a feedback scheme is that it provides one extra dimension to phase space and hence the modified dynamics can be affected by irregular behavior.

Indeed, self-pulsing and deterministic chaos has been reported [2.26] in a single-mode laser fed back by its own output, that is, with the cavity losses modulated by a signal proportional to the output intensity. Chaos due to feedback had already been observed in connection with nonlinear passive systems (either a KDP crystal between crossed polarizers [2.43a] or a long optical fiber in a ring cavity [2.43b]). In both cases the passive system was studied per se, being outside the laser cavity, and thus the laser dynamics was not affected by the feedback configuration.

In Sects. 2.4 and 5 we have shown the onset of chaos in low-dimensional optical systems, in controlled conditions displaying a one-to-one correspondence between experiment results and the predictions of their theoretical model.

Here we show how feeding the laser output back on an intracavity modulator introduces a third degree of freedom leading to chaotic instability. When the feedback loop is so fast that it practically provides an "instantaneously" adapted loss coefficient, it does not modify the phase space topology, which in the case of a class B laser remains two-dimensional. If however the time scale of the feedback loop is of the same order as that of the other relevant variables, the system becomes three dimensional. Such a system is ruled by three first-order equations for the intensity x, population difference z and modulation voltage v. With suitable normalizations (see Appendix 2.A, and notice that here x is the intensity, *not* the field) the equations are

$$\begin{aligned} \dot{x} &= -k_0 x(1 + \alpha \sin^2 v - z) \ , \\ \dot{z} &= -\gamma_{\|}(z - A + xz) \ , \\ \dot{v} &= -\beta(v - B + fx) \ , \end{aligned} \tag{2.22}$$

where $k(v) = k_0(1 + \alpha \sin^2 v)$ is the loss rate modulated by the voltage v, k_0 is the nonmodulated cavity loss parameter, α is a coupling constant, $\gamma_{\|}$ is the population decay rate, and β the damping constant of the feedback loop. Furthermore B is the voltage bias applied to the second input of the modulator amplifier, A is the pump parameter, f is a coupling coefficient between intensity x detected on D and voltage v. Notice that x is normalized to the saturation intensity, z and A to the threshold population (without feedback) and v is given in angular units, that is, if we call V the voltage applied to the modulator and V_0 the $\lambda/2$ modulator voltage, then $v = V/V_0$.

The experimental system of [2.26] has $k_0 = 1.17 \times 10^7\,(\mathrm{s}^{-1})$, $\gamma_{\|} = 0.98 \times 10^4\,(\mathrm{s}^{-1})$, $\beta = 3.0 \times 10^4\,(\mathrm{s}^{-1})$ and a normalized pump $A = 4.2$. The stationary solutions $(\bar{x}, \bar{z}, \bar{v})$ of (2.22) imply the condition

$$B = f\bar{x} + \arcsin\left(\frac{A/\alpha}{1 + \bar{x}} - \frac{1}{\alpha}\right)^{1/2} . \tag{2.23}$$

Depending on the feedback coupling f, for different bias values B we can have mono or bistability (Fig. 2.20). In particular, around $f = 0.1$ we expect an ambiguity, since (2.23) provides a quasi-vertical curve. Indeed as we show later, this is the region where we observe chaos.

By a linear stability analysis around the stationary solution, we evaluate the points where the system starts self pulsing (Hopf bifurcations). The lines of Hopf bifurcations are drawn in Fig. 2.20 (dashed) for three different β values. In fact, we have a slight uncertainty in the assignement of the open loop

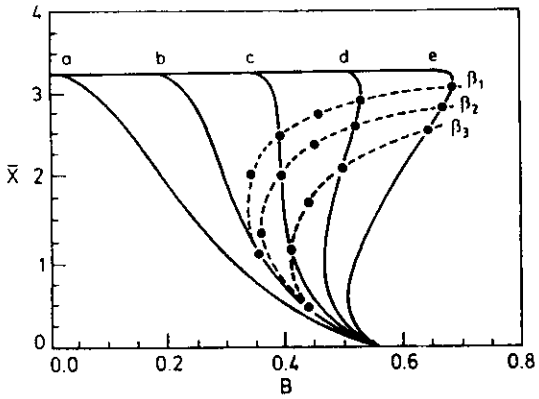

Fig. 2.20. Laser with feedback: Plots of normalised stationary intensity x vs B (the bias-voltage B is expressed in angular units) for different values of the feedback coupling constant f. The curves (a to e) refer to $f = 0$, 0.052, 0.102, 0.152 and 0.202, respectively. (- - -) correspond to the loci of the first Hopf bifurcations for three different values of the damping constant (s^{-1}) of the feedback loop, namely: $\beta_1 = 3.5 \times 10^4$, $\beta_2 = 3.0 \times 10^4$ and $\beta_3 = 2.5 \times 10^4$.

damping constant. At the intersection points of the stationary solutions (lines with fixed f) with the lines of onset of Hopf bifurcations (lines with fixed β) the corresponding pulsing frequency in kHz is given in Table 2.1.

Table 2.1. Laser with feedback: Values [kHz] of the first Hopf bifurcation

$10^{-4} \times \beta$	$f = 0.052$	$f = 0.102$	$f = 0.152$	$f = 0.202$
2.5		31	39	57
3.0	45	16	39	49
3.5	51	15	29	36

In Fig. 2.21 we present the power spectra of the intensity detected in the experiment. Figure 2.21a shows the first Hopf bifurcation, Fig. 2.21b the appearence of a subharmonic $f/2$, and Fig. 2.21c corresponds to the appearence of chaos. Beyond chaos, there are periodic time windows. In order to get full assurance of the chaotic nature of the time plot of Fig. 2.21c, the correlation dimension was measured along the lines already outlined in Sect. 2.3.

Figure 2.22 shows clear evidence of a fractal exponent $D_2 = 2.6 \pm 0.1$. While Fig. 2.22 comes from the experiment, the same D_2 value is obtained by solving numerically (2.22) for $\beta = \beta_2 = 3.0 \times 10^4$ and $B = 0.383$. The theoretical plots, shown in Fig. 2.22, closely follow the experimental ones with uncertainties smaller than the dot sizes. Narrow regions with higher-order subharmonics ($f/4$ and $f/8$) plus $f/3$ windows were observed beyond chaos. In order to have a better understanding of the chaotic scenario, we have solved nu-

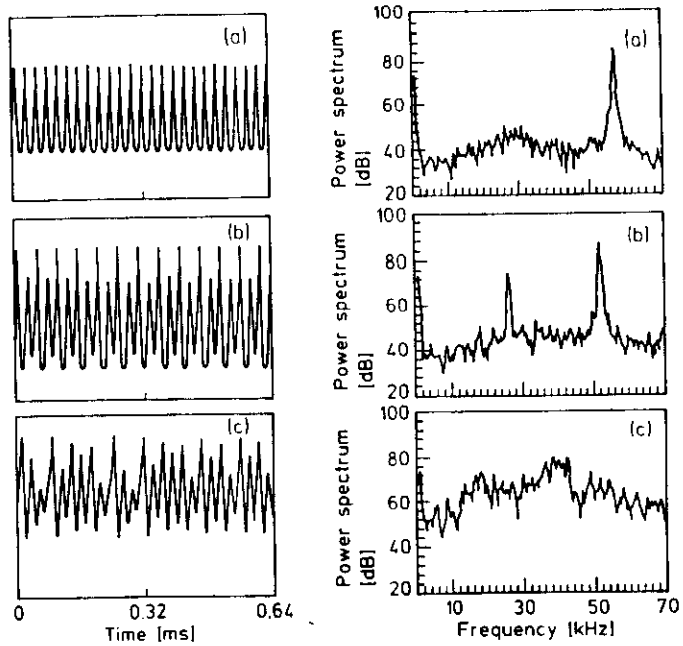

Fig. 2.21a–c. Laser with feedback: Digitizer time plots of the experimental laser intensity (*left*) and the corresponding power spectra (*right*) for increasing values of the control parameter B. (**a**) corresponds to the onset of the first Hopf bifurcation, at a frequency $\nu = 57.3$ kHz, $B = 0.364$; (**b**) shows the appearence of subharmonic bifurctation $f/2$ where the fundamental frequency is $\nu = 52.0$ kHz, $B = 0.378$ and (**c**) shows the appearence of chaos, $B = 0.383$

merically (2.22). An accurate localization of the bifurcation points was done by studying the stability of the phase space orbits in term of their Floquet multipliers. More specifically, the multipliers were evaluated by determining the Poincaré sections with the Henon method [2.26], and finding the zero of the associated recursive relation by the Newton method. In Table 2.2 we give the bifurcation diagram, which shows clear evidence of a Feigenbaum scenario with a Feigenbaum converging ratio in fair agreement with the asymptotic value.

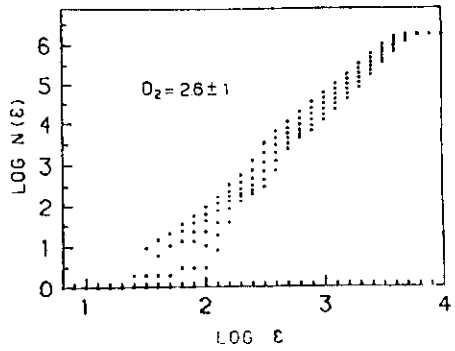

Fig. 2.22. Laser with feedback: Plots of $\log N_n(\varepsilon)$ vs $\log \varepsilon$ for different values of embedding dimension n ($n = 10$–15). Square dots come from experiment. Theoretical plots coincide with the experimental ones within the dot sizes

Table 2.2. Laser with feedback: Bifurcation parameters and Feigenbaum ratio

Bifurcation	B	δ
f	0.394907	
$f/2$	0.395355	
$f/4$	0.395662	...5.11
$f/8$	0.395722	...5.00
chaos	0.395734	

In conclusion, we have shown theoretically and experimentally that the introduction of negative feedback provides a third dynamical degree of freedom sufficient to yield self pulsing and chaotic behavior when the damping constant β of the feedback loop is of the same order as the population decay rate.

2.7 The Bidirectional Ring Laser

Last we consider a longitudinal single mode CO_2 ring laser in which both directions of propagation are allowed [2.25]. The line width being homogeneously broadened, the two counterpropagating beams cannot work at the same time, because they must compete for the same amount of population inversion. Moreover they are slightly detuned between each other - and with respect to line centre – because, for intrinsic asymmetries, cavity losses are different in the two propagation directions (k_1 and k_2); this results in a different mode pulling and then different lasing frequency. Indeed, having a gas flow in the laser tube, this already induces a small amount of Doppler shift in the interaction with one or the other of the two counter-running modes. The detuning has been shown experimentally as well as in the numerical solution to be essential for breaking the symmetry between the two directions. A forbidden gap around the center of the molecular line, as well as the interchange of role of forward and backward fields at right and left of the line center are evidence of such a detuning. If $k_{1,2}$ were the "cold" damping rates, they could not differ for reciprocity (in a passive medium thermodynamics forbids such a symmetry breaking). However the $k_{1,2}$ in the active medium differ for the above-mentioned gas flow effect.

Through the grating induced in the population inversion by the interference of the two waves we have an interchange of energy from one field into the other by backscattering, so that we may consider the system as a LIS (where the injection comes from the counterpropagating-mode).

A modelling of this system has been given in Appendix 2.A.5. Here together with the detuning from the cavity mode we have to take into account two complex running waves and the induces time-dependent grating in the population inversion (truncated at the first order in the expansion). Being x and y the two complex fields, z (real) the spatially uniform component of population inversion, and w the complex amplitude of the grating incuced in the inversion we have from (2.A.28) when losses and pumping are included

$$
\begin{aligned}
\dot{x} &= \frac{1}{1+i\delta}(zx + w^*y) - x \ , \\
\dot{y} &= \frac{1}{1+i\delta}(zy + wx) - \frac{k_2}{k_1}y \ , \\
\frac{k_1}{\gamma_{\|}}\dot{z} &= (z_0 - z) + \frac{1}{1+\delta^2}[z(|x|^2 + |y|^2) + w^*x^*y + wxy^*] \ , \\
\frac{k_1}{\gamma_{\|}}\dot{w} &= -w - \frac{1}{1+\delta^2}[zx^*y + w(|x|^2 + |y|^2)]
\end{aligned}
\tag{2.24}
$$

with δ cavity detuning, z_0 pump parameter and normalized time $\tau = Kt$. Numerical solutions of this seven equation system closely matches all experimental results.

In our parameter space (Fig. 2.23) we can distinguish three main different regions showing completely different behavior. In the first one we observe a self-pulsing very similar to that of the laser with an injected signal. One mode is also running CW while in the other one we observe only spikes, in phase with the main mode, which occur at a repetition rate (ω_S) of the order of $\gamma_{\|}$. In fact, as in the LIS system, the CW working mode injects some energy into the other one letting population inversion increase up to a level at which a giant pulse takes place (the height may be 500 times greater than the stationary level). During the pulse both modes go above threshold and spike in phase. Superimposed to the decay we see relaxation oscillations typical of CO_2 lasers with a frequency (ω_0) very near to Ω : they are out of phase because of competition between the two modes.

For higher excitation currents we observe a deterministic switching due to competition between the two fields with low frequency (30 Hz). During interchange jumps we observe again the two frequencies of Fig. 2.24 but with the lower one increased because of a larger value of $\gamma_{\|}$ (higher current) while the higher one can be varied also by adjusting the cavity length and alignment by moving a mirror mounted on a piezoelectric crystal.

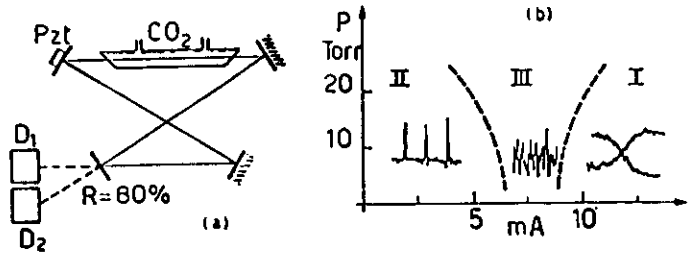

Fig. 2.23a,b. Bidirectional ring laser: **(a)** Experimental set-up: Gain cell with partial pressures: CO_2 1, N_2 1.5 Torr, He variable. Cavity length 4.2 m; PZT piezoelectric mirror translator; D_1 and D_2 detectors for forward and backward intensities. **(b)** Phase diagram for total pressure (P) and discharge current (mA). Regions are: (I) mode alternation, (II) self Q-switch, (III) irregular pulsation

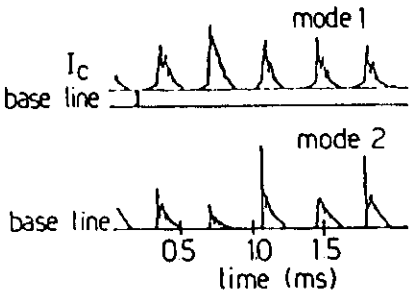

Fig. 2.24. Bidirectional ring laser – Region (*II*): Output intensity vs time. The upper signal has a CW baseline, while the lower oscillates over a zero level. Oscillations relax to the steady state before a new jump (interchange between CW action) takes place

The transition between these two regimes is not abrupt and it takes place through a region which shows chaotic behavior. Here both phenomena related to population inversion, spiking (lower currents) and oscillation (higher currents) take place; effective output frequency results also as a combination of the two others ($\omega_s + \omega_0$). At the same time if we adjust the cavity mirror position so that we brinig $\Omega \simeq (\omega_s + \omega_0)$ we obtain a competition of two different variables (population inversion and field) on the same time scale. The result is a fully developed chaos (Fig. 2.25).

If now we inject back one field into the laser with an external mirror (a fifth mirror in the configuration of Fig. 2.23) we obtain: stabilization of self-spiking, stable laser action instead of switching between the two modes and chaotic behavior. At the boundary between the spiking and the chaotic region we observe a phenomenology typical of a laser with an injected signal (Fig. 2.26). It means that in this situations we have parameters practically equal to those responsible of such behavior in the LIS case, although the system here is more complicated.

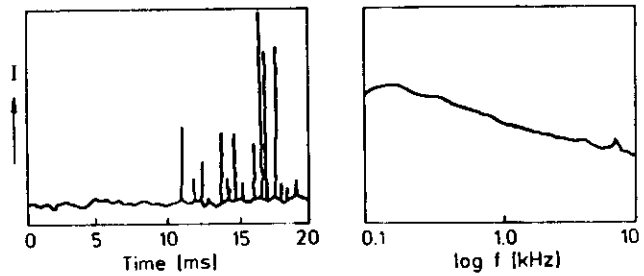

Fig. 2.25. Bidirectional ring laser – Region (*III*): Output intensity vs time for a wholly chaotic signal (*left*). Log-log power spectrum with low frequency divergence $f^{-\alpha}$, $\alpha \simeq 0.6$ (*right*)

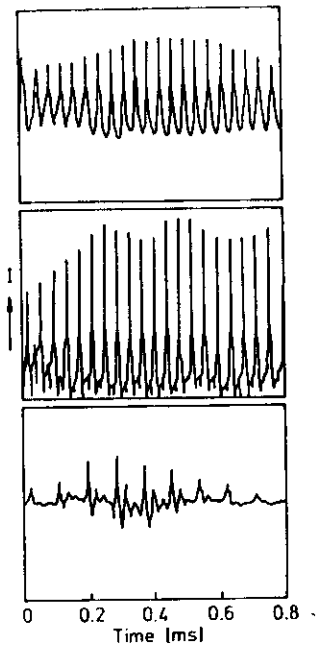

Fig. 2.26. Bidirectional ring with extra mirror to reinject the forward mode into the backward one: Output intensity vs time. Bifurcation sequence in analogy with a laser with injected signal

2.8 Conclusion

We have seen that the single-mode CO_2 laser has a rich phenomenology, which we can reproduce numerically with simple theoretical models.

In experiments involving a parameter modulation or feedback we obtain much more stable and noise-free output so that we can easily compute fractal dimensions and Kolmogorov entropies. At the same time the phenomenology is here not so rich as in experiments where interaction with another field takes place (LIS and bidirectional ring). This must be attributed to the higher complexity of such an interaction where not only an amplitude but also a phase coupling takes place, while in the parameter modulation case interaction is carried only through amplitude modulation.

Summarizing we have found:

i) in a laser with modulated parameters or feedback, a clear Feigenbaum route to chaos, with related δ_F and accumulation point evidence;
ii) in a laser with an injected signal, two different routes to chaos, by intermittency and period doubling;
iii) in a bidirectional ring laser, self-spiking and chaos.

In this last system we find also a surprising coincidence with a laser with an injected signal when we reflect back one mode into the laser.

2.A Appendix: A Simple-Minded Approach to Laser Equations

2.A.1 The Laser Equations

Leaving to textbooks [2.5] a detailed derivation of the laser equations, here we use a pedagogical approach which may appear oversimplified, but which contains the relevant physics. We consider the quantum interaction of a single mode of frequency ω_c described by Bose operators a, a^+, with N non-interacting two-level atoms, each described by Pauli operators $\sigma_i^{\pm}$, σ_{3i} (r_i : position of i-th atom) and with a transition frequency ω_0. The Hamiltonian is

$$\frac{H}{\hbar} = \omega_c a^+ a + \frac{\omega_0}{2}\sum_i \sigma_{3i} + ig\sum_i [a^+ \exp(-ikr_i)\sigma_i - a\exp(ikr_i)\sigma_i^+] \tag{2.A.1}$$

where $g^2 = (\omega_c \mu^2)/(2\hbar\varepsilon_0 V)$ (V : cavity volume, μ : atomic dipole moment). Using the commutation rules

$$\begin{aligned} &[a, a^+] = 1 \\ &[\sigma^+, \sigma^-] = \sigma_3 \\ &[\sigma_3, \sigma^{\pm}] = \pm 2\sigma^{\pm} \end{aligned} \tag{2.A.2}$$

for the same atom, otherwise zero. It is easily seen that the collective operators

$$\begin{aligned} J_3 &= \sum_i \sigma_{3i} \ , \\ J^{\pm} &= \sum_i \sigma_i^{\pm} \exp(\pm ikr_i) \end{aligned} \tag{2.A.3}$$

obey also Pauli commutation rules.

The associated Heisenberg equations of motion can then be written

$$\begin{aligned} \dot{a} &= -i\omega_c a + gJ^- \ , \\ \dot{J}^- &= -i\omega_0 J^- + gaJ_3 \ , \\ \dot{J}_3 &= -2g(a^+ J^- + aJ^+) \ . \end{aligned} \tag{2.A.4}$$

Equations (2.A.4) look formally like the dissipation-less of (2.6). However, their operator means that the corresponding equations for expectation values imply an infinite hierarchy. We truncate it by factoring out expectation values (semi-classical approximation):

$$\langle aJ^+ \rangle \sim \langle a \rangle \langle J^+ \rangle \ .$$

Thus (2.A.4) can be taken as C-number equations, and decorated with the three phenomenological damping rates $-ka$, $-\gamma_\perp J^-$, $-\gamma_\parallel (J_3 - J_0)$, respectively, where J_0 is the inversion imposed by the pump in the absence of field. Recurring to a more familiar notation ($a \to E$, $J^- \to P$, $J_3 \to \Delta$) and considering also an external field E_0 at frequency ω_1, the single-mode Maxwell-Bloch equations are

$$\begin{aligned} \dot{E} &= -(i\omega_c + k)E + gP + kE_0 e^{-i\omega_1 t} \ , \\ \dot{P} &= -(i\omega_0 + \gamma_\perp)P + gE\Delta \ , \\ \dot{\Delta} &= -\gamma_\parallel(\Delta - \Delta_0) - 2g(E^* P + EP^*) \ . \end{aligned} \tag{2.A.5}$$

Equilibrium solutions at resonance ($\omega_c = \omega_0$) and in the absence of external field yield

$$\overline{\Delta} = \frac{\Delta_0}{1 + \overline{E}^2/E_s^2} = \frac{\gamma_\perp k}{g^2} \tag{2.A.6'}$$

where we have called E_s^2 the saturation photon number

$$E_s^2 = \frac{\gamma_\perp \gamma_\parallel}{4g^2} \ . \tag{2.A.6''}$$

It then follows

$$\overline{E} = E_s \sqrt{\frac{\Delta_0}{\overline{\Delta}} - 1} \quad \text{and}$$

$$\overline{P} = \frac{g}{\gamma_\perp}\overline{\Delta}\,\overline{E} \ . \tag{2.A.6'''}$$

To get the order of magnitude, take an allowed visible transition in a dilute gas confined in $V = 1\,\mathrm{cm}^3$ (as, e.g., in He-Ne or A^+ lasers). Then $\gamma_\perp \sim \gamma_\parallel \sim 10^8\,\mathrm{s}^{-1}$ and $E_s^2 \sim 10^8$. Add a cavity 1 m long with 1 % losses, then $k \sim 3 \times 10^6\,\mathrm{s}^{-1}$, and $\overline{\Delta} \sim 3 \times 10^6$ inverted atoms. It is convenient to scale all variables to these parameters, as follows

$$\begin{aligned} x &= E/E_s \ , \\ z &= \Delta/\overline{\Delta} \quad (z_0 = \Delta_0/\overline{\Delta}) \ , \\ y &= P/(\overline{\Delta} E_s g/\gamma_\perp) \ . \end{aligned} \tag{2.A.7}$$

So that the scaled equilibrium values at resonance are

$$\begin{aligned} \bar{x} &= \bar{y} = \sqrt{z_0 - 1} \ , \\ \bar{z} &= 1 \ . \end{aligned} \tag{2.A.8}$$

Let us scale the frequencies as follows

$$\vartheta = \frac{\omega_c - \omega_L}{k} \quad \text{(cavity mistuning)} ,$$
$$\delta = \frac{\omega_0 - \omega_L}{\gamma_\perp} \quad \text{(atomic detuning)} . \tag{2.A.9}$$

Here ω_L is either the frequency ω_1 of the external laser or, in the absence of an external reference, the frequency of the laser field (which does not coincide with the cold cavity ω_c and will be determined later). The scaled equations are

$$\begin{aligned} \dot{x}/k &= -(i\vartheta + 1)x + y + x_0 , \\ \dot{y}/\gamma_\perp &= -(i\delta + 1)y + xz , \\ \dot{z}/\gamma_\parallel &= -z + z_0 - \tfrac{1}{2}(xy^* + x^*y) . \end{aligned} \tag{2.A.10}$$

For $x_0 = 0$, at equilibrium the first and second yield, for $\bar{x} \neq 0$:

$$\bar{z} = (1 + i\theta)(1 + i\delta) . \tag{2.A.11}$$

Since $\bar{z}$ is real, this implies the pulling condition

$$\theta = -\delta . \tag{2.A.12}$$

This assignes the value of ω_L as we see rewriting it as

$$\frac{\omega_c - \omega_L}{k} = \frac{\omega_L - \omega_0}{\gamma_\perp} . \tag{2.A.12'}$$

Setting (2.12) into (2.11) we have the increase in threshold due to detuning

$$\bar{z} = 1 + \delta^2 \tag{2.A.13'}$$

and replacing it into the last of (2.10)

$$|\bar{x}|^2 = z_0 - (1 + \delta^2) . \tag{2.A.13''}$$

Equation (2.13) generalizes (2.8) off resonance.

2.A.2 Adiabatic Elimination of Polarization – Modulation and Injection

Solving (2.10) at equilibrium

$$y = \frac{xz}{1 + i\delta} .$$

Replacing this result into the field and population equations we obtain

$$\begin{aligned} \dot{x}/k &= -(1 + i\vartheta)x + \frac{xz}{1 + i\delta} + x_0 , \\ \dot{z}/\gamma_\parallel &= -z + z_0 - z\frac{|x|^2}{1 + \delta^2} . \end{aligned} \tag{2.A.14}$$

First, take $x_0 = 0$.

For $\theta = \delta = 0$ (resonance) we recover the equations of Sect. 2.3. If $k = k(t)$ we have loss modulation. If $k = \text{const}$, $\delta = \delta(t)$ we have frequency modulation. In the first case, working at resonance, we have a *real* x, and just 3 equations. Indeed, because the first two are non-autonomous, a third equation must be introduced to account for the explicit time dependence

$$k(t) = k_1(1 + m \cos \Omega t) \tag{2.A.15}$$

The three equations are

$$\begin{aligned} \dot{x} &= -k(t)x(1 + z) , \\ \dot{z} &= -\gamma_\parallel(z - z_0 + z|x|^2) , \\ \dot{k} &= -mk_1\Omega \sin \Omega t , \end{aligned} \tag{2.A.16}$$

or equivalently if $I = |x|^2$ the first two (2.16a,b) can be written as

$$\begin{aligned} \dot{I} &= -2kI(1 - z) , \\ \dot{z} &= -\gamma_\parallel(z - z_0 + zI) . \end{aligned} \tag{2.A.17}$$

In the second case the field has two non-zero components, and can not be reduced to a single variable. Writing

$$x = x_1 + ix_2 = \sqrt{I}e^{i\varphi} \tag{2.A.18}$$

it is easily seen that in terms of intensity the equations shown in [2.44] are valid

$$\begin{aligned} \frac{\dot{I}}{k} &= -2I\left(1 - \frac{2}{1 + \delta^2}\right) , \\ \frac{\dot{z}}{\gamma_\parallel} &= z_0 - z - \frac{zI}{1 + \delta^2} , \\ \delta &= \delta(t) . \end{aligned} \tag{2.A.17'}$$

But this is *not* the full story. In fact, a fourth equation for $\varphi(t)$ should be added or, equivalently, the above set must be replaced by

$$\begin{aligned} \frac{\dot{x}}{k} &= -x_1 + \theta x_2 + z\frac{x_1 + \delta x_2}{1 + \delta^2} , \\ \frac{\dot{x}_2}{k} &= -x_2 - \theta x_1 + z\frac{x_2 - \delta x_1}{1 + \delta^2} , \\ \frac{\dot{z}}{\gamma_\parallel} &= -z + z_0 - z\frac{(x_1^2 + x_2^2)}{1 + \delta^2} , \\ \delta &= \delta|x| . \end{aligned} \tag{2.A.19}$$

This shows that, at variance with loss modulation, in case of phase modulation a class B laser seems to be ruled by four equations. However, in the absence of an external field frequency, thus the decomposition (2.18) should be immaterial, since $\varphi = 0$ always. We deal with this problem later when performing a linear stability analysis. For $x_0 \neq 0$, we must add it to (2.19), and redefine θ and δ with respect to ω_1, rather than ω_L. They were written in [2.39] in a slightly different form, because z was there defined as

$$z \to \frac{z}{1+\delta^2} \ .$$

Thus the factor $(1+\delta^2)^{-1}$ present in (2.19) is missing in [Ref. 2.39, Eq. (2.10)].

Notice that keeping x_0 in the 1st of (2.14) makes the equilibrium version ($\dot{x} = 0$) of that equation non homogeneous in $\bar{x}$, hence one can no longer derive the full relation (2.12′). For this, [Ref. 2.39, Eq. (2.14)] is wrong.

2.A.3 Linear Stability Analysis of Class B Solutions

At resonance ($\theta = \delta = 0$) we have two coupled equations, and the deviations from the steady state yield two eigenvalues $\lambda_{1,2}$. For $x_0 = 0$, the steady-state solutions are given by

$$\bar{z} = 1, \quad \bar{I} = |\bar{x}|^2 = z_0 - 1 \ .$$

Writing $I = \bar{I} + u$, $z = \bar{z} + v$, we have from (2.17)

$$\begin{aligned} \dot{u} &= 2k(z_0 - 1)v \ , \\ \dot{v} &= -\gamma_{\|} u - \gamma_{\|} z_0 v \ . \end{aligned} \tag{2.A.20}$$

Thus the eigenvalues λ correspond to

$$\begin{aligned} \lambda &= -\frac{\gamma}{2} z_0 \pm i\sqrt{2k\gamma_{\|}(z_0 - 1) - \frac{\gamma^2}{4} z_0^2} \\ &\approx -\frac{\gamma}{2} z_0 \pm i\sqrt{2k\gamma_{\|}(z_0 - 1)} \end{aligned} \tag{2.A.21}$$

since $\gamma_{\|} \ll k$.

Equation (2.21) shows that a disturbance in a class B laser decays over a time scale $1/\gamma_{\|}$ (assume z_0 and $z_0 - 1$ of the order of 1, for simplicity) and it has a ringing with period $1/\sqrt{k\gamma_{\|}}$. We remember that for a CO_2-laser the two time scales are, respectively, 10^{-3} s and 10^{-5} s.

If now we consider a non-zero detuning, but still $x_0 = 0$ the equations are given by (2.10) or equivalently by the first two of (2.17′) plus a third equation for phase φ. Indeed, writing x as in (2.18), we have for the phase $\varphi = \arctan x_2/x_1$,

$$\frac{\dot{\varphi}}{k} = \frac{1}{kI}(x_1 \dot{x}_2 - x_2 \dot{x}_1) = -\theta + \frac{\delta}{1+\delta^2} z \ . \tag{2.A.22}$$

At equilibrium $\varphi = 0$, since $\theta = \delta$. Notice that having chosen a frame rotating at the frequency ω_L of the laser field, by definition $\varphi = 0$ always, hence the extended stability analysis should provide a third root $\lambda = 0$. Indeed, extending the analysis of (2.20) for $\delta \neq 0$ we obtain three linear equations (we use the matrix form)

$$\begin{pmatrix} \dot{u}/k \\ \dot{v}/\gamma \\ \dot{\varphi}/k \end{pmatrix} = \begin{pmatrix} 0 & 2\left(\frac{z_0}{1+\delta^2} - 1\right) & 0 \\ -1 & -\frac{z_0}{1+\delta^2} & 0 \\ 0 & -\frac{\delta}{1+\delta^2} & 0 \end{pmatrix} \begin{pmatrix} u \\ v \\ \varphi \end{pmatrix} \tag{2.A.23}$$

and the corresponding roots of $\tilde{M} - \lambda \tilde{I} = 0$ are again the two given by (2.21) plus $\lambda_3 = 0$, thus showing that the phase is irrelevant.

In presence of modulation, for a small modulation index, the motion is a periodic orbit at the frequency of the external perturbation, around the stationary values $\bar{I}$, $\bar{z}$, and with a radius linear in the perturbation. The stability of this synchronous orbit has to be tested by Floquet theory [2.34].

2.A.4 Laser with Injected Signal (LIS)

The equations are (2.19a–c), with the addition of x_0 to the first one. These equations have been discussed in [2.39]. Alternatively, writing $x = \sqrt{I}\exp(i\varphi)$, we have two equations for I and φ, so that the full set of LIS equations can be written as

$$\begin{aligned} \dot{I}/2k &= \frac{Iz}{1+\delta^2} - I + \sqrt{I} x_0 \cos\varphi \ , \\ \dot{\varphi}/k &= -\theta - \frac{\delta}{1+\delta^2} z - \frac{x_0}{\sqrt{I}} \sin\varphi \ , \\ \dot{z}/\gamma_{\|} &= z_0 - z - \frac{zI}{1+\delta^2} \ , \end{aligned} \tag{2.A.24}$$

where, we recall that θ and δ are defined with reference to the external frequency ω_1. At equilibrium calling $I_0 = x_0^2$, we have the relation

$$I_0 = \bar{I}\left[\left(\theta + \frac{\delta z_0}{1+\delta^2+\bar{I}}\right)^2 + \left(\frac{z_0}{1+\delta^2+\bar{I}} - 1\right)^2\right] \tag{2.A.25}$$

which, yields the curves of Fig. 2.16 showing bistability. In [2.39] one can find an extended stability analysis yielding the three roots of the linearized (2.24).

2.A.5 The Bidirectional Class B Ring Laser

When two counterpropagating fields $a\exp[-i(\omega t - kr)] + \text{c.c.}$ and $b\exp[-i(\omega t + kr)] + \text{c.c.}$ coexist as separate dynamical variables, then

$$[a, b^+] = 0$$

and we have a bidirectional ring. The corresponding Hamiltonian is

$$\frac{H}{\hbar} = \frac{\omega_0}{2}\sum \sigma_{3i} + \omega(a^+a + b^+b) - ig\sum_i [\sigma_i^+(ae^{ikr_i} + be^{-ikr_i}) - \sigma_i^-(a^+e^{-ikr_i} + b^+e^{ikr_i})] \quad (2.A.26)$$

We now introduce a whole class of k-dependent collective operators, which are Fourier transforms of the position-dependent single-atom operators, defined as follows

$$J^{\pm}(k) = \sum \sigma_i^{\pm} e^{\pm ikr_i} ,$$
$$J_3(k) = \sum \sigma_{3i} e^{ikr_i} .$$

It is easily verified that

$$[J^+(k), J^-(-k)] = J_3(0) ,$$
$$[J_3(0), J^{\pm}(k)] = \pm 2J^{\pm}(k) ,$$

and furthermore

$$[J^+(k), J^-(k)] = J_3(2k) ,$$
$$[J_3(2k), J^+(k)] = 2J^+(3k) , \quad (2.A.27)$$

and so on.

One immediately sees that the Heisenberg equations for fields are

$$\dot{a} = -i\omega a + gJ^-(-k) ,$$
$$\dot{b} = -i\omega b + gJ^-(k) .$$

Adiabatic elimination of polarization yields for single atom

$$\sigma^- = \frac{g\sigma_3}{\gamma_\perp + i\Delta\omega}(ae^{-ikr_i})$$

where $\Delta\omega = \omega_0 - \omega$.

Multiplying both sides for $\exp(-ikr_i)$ one builds a relation for $J^-(-k)$. This way we build the following equations

$$\dot{a} = -\frac{g^2}{\gamma_\perp + i\Delta\omega}[aJ_3(o) + bJ_3(-2k)] ,$$
$$\dot{b} = -\frac{g^2}{\gamma_\perp + i\Delta\omega}[aJ_3(2k) + bJ_3(0)] ,$$
$$\dot{J}_3(0) = \frac{4g^2}{\gamma_\perp^2 + \Delta\omega^2}[J_3(0)(|a|^2 + |b|^2) + J_3(2k)ab^+ + J_3(-2k)a^+b] ,$$
$$\dot{J}_3(2k) = \frac{4g^2}{\gamma^2 + \Delta\omega^2}[J_3(2k)(|a|^2 + |b|^2) + J_3(4k)ab^+ + J_3(0)a^+b] , \quad (2.A.28)$$

and similar for $\dot{J}_3(-2k)$. There is a hierarchy built from the third equation, scaling upward (or downward) the k arguments by $2k$ at each step. If we introduce a one-dimensional lattice, with site i corresponding to $2ki$, then we have $J_3(i)$ coupled with $J_3(i\pm1)$. The above equations have to be considered as classical, and completed with phenomenological damping terms. Truncation problems are discussed in Sect. 2.7. If we set $J_3(4k) \approx 0$, already (2.28) is a set of 7 real closed equations: two each for a and b, one for $J_3(0)$ and two for $J_3(\pm 2k)$.

Acknowledgement. I must express my appreciation and gratitude to all colleagues and students with whom I have been collaborating over the past years, and with whom I have shared the excitement of discovering new "whats" and "hows" and understanding the "whys". The reason why I had to prepare this manuscript alone is that most of them are now scattered around the world in different Laboratories. Let me list them in alphabetic order (their individual contributions appear from the References): N.B. Abraham, R. Badii, A. Califano, W. Gadomski, G.L. Lippi, F. Lisi, R. Meucci, A. Poggi, A. Politi, G.P. Puccioni, N. Ridi, J.R. Tredicce and L. Ulivi.

Part of this research was supported by the EJOB project of European Economic Community.

References

2.1 W.E. Lamb Jr.: Phys. Rev. **134**, A1429 (1964)
2.2 H. Haken: *Laser Theory*, Corr. Printing (Springer, Berlin, Heidelberg 1984)
2.3 M. Scully, W.E. Lamb Jr.: Phys. Rev. Lett. **16**, 853 (1966), Phys. Rev. **159**, 208 (1967); and **166**, 246 (1968)
2.4 J.P. Gordon: Phys. Rev. **161**, 367 (1967)
2.5 H. Haken: *Synergetics*, 3rd ed., Springer Ser. Syn., Vol. 1 (Springer, Berlin, Heidelberg 1983)
2.6 F.T. Arecchi: In *Order and Fluctuations in Equilibrium and Nonequilibrium Statistical Mechanics* (Proc. XVII Solvay Conf. on Physics) ed. by G. Nicolis et al. (Wiley, New York 1981) p. 107
2.7 R.J. Glauber: In *Quantum Optics and Electronics*, ed. by D. De Witt et al. (Gordon and Breach, New York 1965)
2.8 F.T. Arecchi: In *Quantum Optics*, ed. by R.J. Glauber (Academic, New York 1969)
2.9 J.P. Eckmann: Rev. Mod. Phys. **53**, 643 (1981); J.P. Eckmann, D. Ruelle: Rev. Mod. Phys. **57**, 617 (1985)
2.10 F.T. Arecchi, V. Degiorgio, B. Querzola: Phys. Rev. Lett. **19**, 1168 (1967)
2.11 J.S. Langer: In *Flucutations, Instabilities and Phase Transitions*, ed. by T.Riste (Plenum, New York 1975)
2.12 H. Risken, H.D. Vollmer: Z. Physik **201**, 323 and **104**, 240 (1967)
2.13 F.T. Arecchi, V. Degiorgio: Phys. Rev. **A3**, 1108 (1971)
2.14 F.T. Arecchi, A. Politi: Phys. Rev. Lett. **45**, 1215 (1980)
2.15 F.T. Arecchi, A. Politi, L. Ulivi: Nuovo Cimento **71B**, 119 (1982)
2.16 Q.H.F. Vrehen, H.M. Gibbs: In *Dissipative Systems in Quantum Optics*, ed. by R. Bonifacio, Topics Curr. Phys., Vol. 27 (Springer, Berlin, Heidelberg 1982) p. 111
2.17 F. Haake, J. Haus, H. King, G. Schröder, R. Glauber: Phys. Rev. Lett. **45**, 558 (1980) and Phys. Rev. **A23**, 1322 (1981)
2.18a W. Lange, F. Mitschke, R. Deserno, J. Mlynek: Phys. Rev. **32A**, 1271 (1985)
2.18b E.Arimondo, C.Gabbanini, A. Gozzini, R. Longo, F. Maccarrone, F. Mango, E. Menchi: In *Optical Bistability III*, ec. by H.M. Gibbs et al., Springer Proc. Phys. 8, 256-259 (Springer, Berlin, Heidelberg 1986)
2.19 E.M. Lorenz: J. Atmos. Sci. **20**, 130 (1963)

2.20 P. Cvitanovich (ed.): *Universality in Chaos* (Hilger, Bristol 1984)
2.21 L.M. Hoffer, T.H. Chyba, N.B. Abraham: J. Opt. Soc. Am. **B2**, 102 (1985)
2.22 L.W. Casperson: J. Opt. Soc. Am. **B2**, 62 (1985)
2.23 F.T. Arecchi, G.L. Lippi, G.P. Puccioni, J.R. Tredicce: Opt. Commun. **51**, 308 (1984)
2.24 F.T. Arecchi, R. Meucci, G.P. Puccioni, J.R. Tredicce: Phys. Rev. Lett. **49**, 1217 (1982)
2.25 G.L. Lippi, J.R. Tredicce, N.B. Abraham, F.T. Arecchi: Opt. Commun. **58**, 129 (1985)
2.26 F.T. Arecchi, W. Gadomski, R. Meucci: Phys. Rev. **A34**, 1617 (1986)
2.27 J.D. Farmer: Physica **4D**, 366 (1982)
2.28 B.B. Mandelbrot: *The Fractal Geometry of Natur* (Freeman, San Francisco 1982)
2.29 P. Grassberger, I. Procaccia: Phys. Rev. Lett. **50**, 346 (1983)
2.30 T. Geisel, J. Niewetberger: Phys. Rev. Lett. **48**, 7 (1982)
2.31 F.T. Arecchi, F. Lisi: Phys. Rev. Lett. **49**, 94 (1982); and **50**, 1328 (1983)
2.32 F.T. Arecchi, R. Badii, A. Politi: Phys. Lett. **103A**, 3 (1984);
F.T. Arecchi, R. Badii, A. Politi: Phys. Rev. **A32**, 402 (1985)
2.33 F.T. Arecchi, A. Califano: Europhysics Lett. **3**, 5 (1987)
2.34 G. Ioos, D.D. Joseph: *Elementary Stability and Bifurcation Theory* (Springer, Berlin, Heidelberg 1980)
2.35 G.P. Puccioni, A. Poggi, W. Gadomski, J.R. Tredicce, F.T. Arecchi: Phys. Rev.Lett. **55**, 339 (1985)
2.36 P. Grassberger: J. Stat. Phys. **26**, 173 (1981)
2.37 L. Lugiato, L.M. Narducci, D.K. Bandy, C.A. Pennise: Opt. Commun. **46**, 64 (1983)
2.38 D.K. Bandy, L.M. Narducci, L. Lugiato: J. Opt. Soc. Am. **B2**, 248 (1985)
2.39 J.R. Tredicce, F.T. Arecchi, G.L. Lippi, G.P. Puccioni: J. Opt. Soc. Am. **B2**, 173 (1985)
2.40 J.L. Boulnois, P. Cottin, A. Van Lenberghe, F.T. Arecchi, G.P. Puccioni: Opt. Commun. **58**, 124 (1986)
2.41 See, e.g., Instruction Manuals of current Argon or Kripton lasers commercially supplied by Coherent or Spectra Physics
2.42 H.A. Haus, Y. Yamamoto: MIT Workshop on Squeezed States of Light,Cambridge, Mass. (21 October 1985) unpublished;
S. Machida, Y. Yamamoto: Opt. Commun. **57**, 290 (1986)
2.43 F.A. Hopf, B.L. Kaplan, H.M. Gibbs, R.L. Shoemaker: Phys. Rev. **A25**, 2172 (1982);
H. Nakatsuka, S. Asaka, H. Itoh, K. Ikeda, M. Matsuoka: Phys. Rev. Lett. **50**, 109 (1983)
2.44 T. Midavaine, D. Dangoisse, P. Glorieux: Phys. Rev. Lett. **55**, 1989 (1985)